

# An Ultraviolet through Infrared Look at Star Formation and Super Star Clusters in Two Circumnuclear Starburst Rings<sup>1</sup>

Dan Maoz<sup>2</sup>

Department of Astronomy, Columbia University, 550 W. 120th St., New York, NY 10027

Aaron J. Barth

Harvard-Smithsonian Center for Astrophysics, 60 Garden Street, Cambridge, MA 02138

Luis C. Ho

The Observatories of the Carnegie Institution of Washington, 813 Santa Barbara St.,  
Pasadena, CA 91101

Amiel Sternberg

School of Physics & Astronomy, Tel-Aviv University, Tel-Aviv 69978, Israel

and

Alexei V. Filippenko

Department of Astronomy, University of California, Berkeley, CA 94720-3411

## ABSTRACT

We present broad-band ( $U$ ,  $V$ ,  $I$ , and  $H$ ) and narrow-band ( $H\alpha$ + $[N\ II]$  and  $Pa\alpha$ ) images of the circumnuclear starburst rings in two nearby spiral galaxies, NGC 1512 and NGC 5248, obtained with the WFPC2 and NICMOS cameras on *HST*. Combined with previously published ultraviolet (UV) *HST* images at 2300 Å, these data provide a particularly wide wavelength range with which to study the properties of the stellar populations, the gas, and the dust in the rings. The young star clusters and the line-emitting gas have different spatial distributions, with some large (50-pc scale) line-emitting regions that have little associated continuum emission, but a  $Pa\alpha$  equivalent width indicating a few-Myr-old embedded stellar population. The observed  $H\alpha/Pa\alpha$  intensity ratios suggest the gas is mixed with dust, making it effective at obscuring some of the young

---

<sup>1</sup>Based on observations with the *Hubble Space Telescope* which is operated by AURA, Inc., under NASA contract NAS 5-26555.

<sup>2</sup> Permanent Address: School of Physics & Astronomy and Wise Observatory, Tel-Aviv University, Tel-Aviv 69978, Israel.

clusters. We identify the major (about 500 in each galaxy) compact continuum sources (super star clusters and individual stars) and analyze their spectral energy distributions (SEDs) from  $0.2\ \mu\text{m}$  to  $1.6\ \mu\text{m}$  by fitting them with a grid of spectral synthesis models with a range of ages and dust extinction. Most of the visible clusters are only mildly reddened, with  $A_V = 0$  to 1 mag, suggesting that the processes that clear out the gas and dust of the stellar birth clouds are efficient and fast. The patchiness of the dust distribution makes it difficult to reliably estimate the star formation rate, based on UV continuum slope or hydrogen emission-line ratios, in starbursts such as these. The cluster SEDs are consistent with a range in ages, from 1 Myr to 300 Myr, but with only a minority older than a few tens of Myr. We point out an age bias, the result of the steep luminosity function of the clusters combined with the fading of clusters as they age, which causes young clusters to be over-represented at any luminosity. Accounting for this bias, the fraction of old clusters is consistent with continuous star formation in the rings over the past  $\sim 300$  Myr. Due to the uncertainties in dating the clusters, we cannot rule out episodic,  $\sim 20$  Myr-long bursts of star formation, but the presence of UV-bright rings in about 10% of spiral galaxies argues against this possibility. Although most of the observed SEDs are well fit by a range of models, some of the brightest young clusters have excess emission in the IR that is not predicted by the models and may be thermal re-radiation by circumstellar dust. The cluster mass functions follow a power-law distribution with index  $-2$ , similar to that recently derived for the starburst in the merging Antennae galaxies, and extending to  $\sim 10^5 M_\odot$ . The lack of a mass scale means that subsequent evolution of the mass function is required, if some of the SSCs are to evolve into globular clusters. The clusters are spatially unresolved or marginally resolved, corresponding to  $V$ -band Gaussian radii of less than a few pc, at an assumed distance of 10 Mpc. In NGC 5248, we report a previously-unknown, 60-pc-radius, inner emission-line ring, and in NGC 1512, a peculiar compact ( $0.1''$  diameter) source with an  $\text{H}\alpha + [\text{N II}]$  equivalent width of  $\sim 7000\ \text{\AA}$ , which may be a so-called Balmer-dominated supernova remnant.

*Subject headings:* galaxies: individual (NGC 1512, NGC 5248) – galaxies: star clusters – galaxies: starburst

## 1. Introduction

Galaxy imaging with the *Hubble Space Telescope* (*HST*) has revealed a population of compact, young star clusters in a variety of starburst environments (Holtzman et al. 1992; Benedict et al. 1993; Whitmore et al. 1993; Conti & Vacca 1994; Hunter, O’Connell, & Gallagher 1994; O’Connell, Gallagher, & Hunter 1994; O’Connell et al. 1995; Whitmore & Schweizer 1995; Meurer et al. 1995; Barth et al. 1995; Maoz et al. 1996; Holtzman et al. 1996; Miller et al. 1997; Stiavelli et al. 1998; Carlson et al. 1998, 1999; Whitmore et al. 1999; Alonso-Herrero et al. 2000; Drissen et al. 2000; Gallagher, Homeier, & Conselice 2000a; Gallagher et al. 2000b; Hunter et al. 2000). These include cooling-flow galaxies, interacting/merging galaxies, “amorphous” peculiar galaxies, and galaxies with circumnuclear star-forming rings. Although such clusters were known previously from ground-based and infrared observations (e.g., Arp & Sandage 1985; Tacconi-Garman, Sternberg, & Eckart 1996), *HST* has vastly increased the number of known objects and the wavelength range and distance to which they can be studied. The *HST* resolution has also allowed measurements demonstrating the compactness of the clusters.

The more luminous among the clusters ( $M_V < -10$  mag [ $L_V > 1.3 \times 10^6 L_{V\odot}$ ], according to some conventions, though the limit is somewhat arbitrary and wavelength dependent) are sometimes termed “super star clusters” (SSCs). The small radii, high luminosities, and presumably high masses of these clusters have led to suggestions that they may remain as bound systems and therefore could be young globular clusters. This view has been reinforced by velocity-dispersion measurements of several bright SSCs (Ho & Filippenko 1996a,b; Smith & Gallagher 2000). Sternberg (1998) has questioned the ultimate globular cluster fate of some of these SSCs. More general debates of the relation between SSCs and globular clusters based on their statistical properties can be found in van den Bergh (1995, 2000), Meurer (1995), Elmegreen & Efremov (1997), Zhang & Fall (1999), and Kroupa, Aarseth, & Hurley (2001). Recently, new views of SSCs are emerging from infrared (IR) and radio observations of dense regions in starburst galaxies that may be very young SSCs, still embedded in their molecular clouds (Smith et al. 1999; Kobulnicky & Johnson 1999; Turner et al. 1999, 2000; Beck, Turner, & Kovo 2000). Learning more about SSCs can shed light on rapid star formation, globular-cluster formation, and the possible connections between them.

Circumnuclear star-forming rings in barred spirals comprise possibly the most numerous class of nearby starburst regions, and offer us an opportunity to study starburst properties at a level of detail that would be impossible for more distant or more heavily obscured systems. The large-scale morphologies and properties of many circumnuclear rings have been studied extensively from the ground (e.g., Hummel et al. 1987; Pérez-Ramírez et al.

2000), but the small sizes of the rings (typically  $\sim 10''$  for nearby galaxies) require the capabilities of *HST* for studies of their detailed structure. Images with WFPC, WFPC2, and FOC have revealed large populations of SSCs in several circumnuclear rings in nearby galaxies (Benedict et al. 1993; Barth et al. 1995; Meurer et al. 1995; Maoz et al. 1996; Buta, Crocker, & Byrd 1999). These clusters, barely resolved by *HST*, have effective radii of only 2–4 pc, and luminosities that range as high as  $M_V = -14$  to  $-15$  mag. As in other environments, if such luminous clusters survive as bound entities for  $10^{10}$  years, they will have magnitudes comparable to those of old Galactic globular clusters today. Circumnuclear rings represent the only known environment in morphologically normal galaxies in which SSCs are found in abundance. Furthermore, analysis of ultraviolet (UV) *HST* images of five such circumnuclear rings indicates that much of the massive star formation in the starburst regions must occur within the compact clusters (Maoz et al. 1996).

Measuring the masses and ages of SSCs is an important step toward understanding their future evolution and determining whether they are similar to young globular clusters. Earlier *HST* studies of star clusters in circumnuclear rings (Benedict et al. 1993; Barth et al. 1995) were based mostly on single-filter images, and the resulting interpretation of the cluster properties was uncertain. Maoz et al. (1996) used an *HST* optical image of the circumnuclear ring in NGC 2997, along with a UV (2300 Å) exposure, to show that with two bands (i.e., a UV-optical color), meaningful lower limits on the masses and upper limits on the extinctions and ages of the clusters could be set.

Recently, Buta et al. (2000) presented *HST* WFPC2 images in five broad UV and optical bands and in  $H\alpha$  of the circumnuclear ring in NGC 1326, another nearby barred early-type spiral galaxy. Comparing their data for the numerous individual detected clusters to spectral synthesis models, they derived a continuum of ages from 5 Myr to 200 Myr, but with 80% to 90% of the clusters being younger than 50 Myr, and typically moderate visual extinctions of 0.6–0.9 mag. The derived masses of the clusters go up to  $5 \times 10^5 M_\odot$ . They also noted that many of the H II regions were devoid of continuum sources, and concluded that the embedded clusters must have high extinctions,  $A_V > 2.5$  mag.

NGC 1512 and NGC 5248 (Hubble types SBab and SABbc, respectively) are two circumnuclear ring galaxies that were included in the Maoz et al. (1996) FOC UV (2300 Å) imaging survey. Distances to these nearby galaxies (heliocentric velocities  $v_h = 911$  and  $1156$  km s $^{-1}$ , respectively) are not accurately known, but are of order 10 Mpc. Maoz et al. detected 43 SSCs in NGC 1512 and 46 in NGC 5248, with similar apparent brightness distributions. Here we describe subsequent broad-band (approximately  $U$ ,  $V$ ,  $I$ , and  $H$ ) and narrow-band ( $H\alpha$ + $[N\text{ II}]$  and  $P\alpha\alpha$ ) *HST* images of these galaxies with WFPC2 and NICMOS. These observations probe for the first time the spectral energy distribution (SED)

of SSCs over such a wide wavelength interval. Apart from providing stronger constraints than before on the physical parameters of the clusters, they have the potential to reveal a large population of clusters that is obscured by dust. Such an obscured population may be younger than that which is detectable at shorter wavelengths, which select only the clusters that have blown off, or emerged from, their birth clouds. The hydrogen emission-line observations provide a direct probe of the ionizing flux from massive stars, and the  $H\alpha/Pa\alpha$  ratio is a useful reddening diagnostic. These observations can therefore give a more complete picture of SSC properties and evolution than previously possible. Both galaxies are at high Galactic latitude and hence undergo little Galactic reddening ( $E[B - V] = 0.02$  mag for NGC 1512 and 0.01 mag for NGC 5248; Schlegel, Finkbeiner, & Davis 1998); we will neglect these small Galactic extinction corrections.

In §2, below, we describe the observations and data reduction. In §3, we analyze the reduced images. We discuss our results and summarize the main conclusions in §4.

## 2. Observations and Reduction

WFPC2 images were taken through the F336W, F547M, F814W, and F658N filters (which correspond loosely to  $U$ ,  $V$ ,  $I$ , and  $H\alpha+[N\ II]\ \lambda\lambda 6548, 6583$ ). The center of each galaxy was positioned on the PC CCD. The rings, which have diameters of  $15''$  and  $11''$  in NGC 1512 and NGC 5248, respectively, fit well on the  $34'' \times 34''$  PC field of view. Integrations were split into sub-exposures to allow cosmic-ray event rejection. The dates and total exposure times are listed in Table 1. The individual images were processed by the standard Space Telescope Science Institute (STScI) pipeline (Biretta et al. 1996), which included bias subtraction and flat-fielding. We combined the sub-exposures using the STSDAS CRREJ task in IRAF<sup>3</sup> to correct for cosmic-ray hits.

NICMOS Camera-2 images were taken through the F160W, F187W, and F187N filters. The F160W filter has an effective wavelength of  $1.6\ \mu\text{m}$ , at the minimum of the background due to zodiacal light and thermal emission from the telescope. The  $Pa\alpha$  line from these two galaxies falls well within the 1% width of the F187N filter. F187W is a broad-band filter centered at  $1.87\ \mu\text{m}$  and was used to provide a measurement of the continuum underlying  $Pa\alpha$ . The Camera-2 field of view is  $19'' \times 19''$ , also accommodating the full diameter of the rings. At the wavelengths of the bandpasses we used, the Camera-2 resolution

---

<sup>3</sup>IRAF (Image Reduction and Analysis Facility) is distributed by the National Optical Astronomy Observatories, which are operated by AURA, Inc., under cooperative agreement with the National Science Foundation.

approximately matches the telescope diffraction limit of  $0.14''$ , corresponding to 7 pc at a distance of 10 Mpc.

For each galaxy-filter combination, the NICMOS observations were split into four equal exposures, between which the telescope was dithered in a “square” pattern with a step size of  $0.5''$ , to allow subsequent elimination of the effects of bad pixels in the detector. Each individual exposure was read with 18 non-destructive readouts in MULTIACCUM mode with the STEP64 temporal sampling sequence. This sequence involves logarithmically growing readout intervals up to 64 s, followed by evenly spaced intervals of 64 s for the remainder of the exposure. The MULTIACCUM mode produces a large dynamic range and the ability to reject cosmic-ray events. The NICMOS images were also reduced by the STScI pipeline processing system, which includes bias-level subtraction, nonlinearity correction, dark-image subtraction, flat-fielding, cosmic-ray rejection, and combination of the individual dithered exposures. The pipeline-reduced narrow-band F187N images of NGC 1512 have a low count rate and show the “pedestal” feature common in NICMOS images, which results from improper bias-level subtraction. We re-reduced these images with STSDAS in IRAF, including the BIASSEQ and PEDSKY tasks to treat the pedestal feature. Although this improved the final results, some remaining background offset in one of the four NICMOS quadrants was removed by adding a constant to the counts in that quadrant.

Photometric calibrations for each camera and filter, as listed in Table 1, were used to convert count rates to physical flux units. The inverse sensitivities for the broad and medium-band filters are the latest circulated by STScI, for a source that has a constant spectrum in  $f_\lambda$ . The inverse sensitivities of the two narrow-band filters were obtained by multiplying the inverse sensitivities for a continuum source in these filters by their effective bandwidths. The effective bandwidths were calculated by integrating over wavelength the filter/system throughput curves and dividing by the throughput at the redshifted wavelengths of the lines for each galaxy. For NGC 5248, Pa $\alpha$  is on the falling part of the filter/system throughput curve, where the transmission is 15% to 35% lower than at peak, for line-emitting gas with velocity of  $\pm 100 \text{ km s}^{-1}$  in the galaxy’s frame. As a result, its inverse sensitivity value is higher than that of NGC 1512, and is uncertain, for a given line-emitting region, by  $\pm 15\%$ . The effective bandwidths are  $39.5 \text{ \AA}$  for F658N,  $213 \text{ \AA}$  for F187N in NGC 1512, and  $275 \text{ \AA}$  for F187N in NGC 5248. We note that, in general, the effective bandwidth is significantly larger than the full width at half maximum (FWHM), or other filter widths appearing in the image headers and in STScI documentation.

In our analysis, we also use the *HST* FOC  $f/96$  F220W images of these galaxies presented and analyzed by Maoz et al. (1996). F220W is a broad-band filter centered at

2300 Å. See Maoz et al. (1996) for full details of those data.

To produce continuum-subtracted  $\text{Pa}\alpha$  images, we “blinked” the F187N and F187W NICMOS exposures and verified that they were well aligned (i.e., the telescope pointing did not change between filters, to within the resolution limits). For each galaxy, we then scaled the F187W image by the ratio of the inverse sensitivities of the F187N and F187W filters, and subtracted it from the F187N image. The  $\text{Pa}\alpha$  emission in these galaxies comes from relatively extended regions having weak continuum emission (see below). The central wavelengths of the two filters are the same, and the continuum makes only a small contribution to the F187N bandpass in these regions. Consequently, we find that the difference images are insensitive to the exact method of continuum subtraction, and there is no need to perform higher-order corrections (e.g., to account for the slope of the continuum by utilizing the F160W images).

We used combinations of scaled versions of the F547M and F814W WFPC2 images to produce continuum images at 6580 Å for each galaxy, for subtraction from the F658N images. The scaling and relative weights were calculated from the central wavelengths, the inverse sensitivities, and the relative exposure times in the three filters, and we found that this gives a good continuum subtraction, without artifacts such as conspicuous negative-flux regions. As with the  $\text{Pa}\alpha$  images, the good subtraction is a result of the mutual avoidance of stellar and emission-line light in these galaxies.

Quillen & Yukita (2000) recently presented an analysis of some of these data. Their work concentrates only on the emission-line data for just one of the galaxies discussed here (NGC 1512), and on the relations between reddening, gas density, and metallicity. Instead of the effective bandwidths, they apparently used the plateau width for the F658N filter and the FWHM for the F187N filter in calibrating the narrow-band images of NGC 1512. Their  $\text{H}\alpha$  fluxes are therefore underestimated by 40% and their  $\text{Pa}\alpha$  fluxes by 11%. In their reduction, they used the F160W image for  $\text{Pa}\alpha$  continuum subtraction. Apart from the relatively large wavelength difference, which may compromise the accuracy of their continuum subtraction, the mismatch between the point-spread functions (PSFs) in the F160W and F187N bands is apparent from their figure.

To enable tracking the SED of individual sources from the UV to the IR, and for constructing ratios of images in different bands, we performed a careful alignment of the images. All images of a galaxy were registered with the F547M image. This was done by “blinking” a given image and the F547M image, and marking the coordinates of the brightest isolated clusters appearing in the two bands. This proved to be fairly challenging for bands far from the F547M band, due to the diverse colors of the clusters (e.g., some clusters that are bright in  $V$  are barely visible at  $1.6\ \mu\text{m}$ , and difficult to identify among the

myriad of IR sources that emerge at longer wavelengths). The cluster coordinates were used to calculate a transformation between images using the GEOMAP task in IRAF, allowing for rotation, translation, and scaling, and the GEOTRAN task was used to apply the transformations to the images. The emission knots in the  $\text{Pa}\alpha$  image are extended and, as mentioned above, not coincident with the clusters seen in the continuum bands. However, since all the NICMOS exposures of each galaxy were already well aligned (including the F187N exposure, which includes continuum emission), the F160W transformation was applied to the continuum-subtracted  $\text{Pa}\alpha$  image. Blinking between the optical and the transformed IR images shows that the registration is not perfect, due to local distortions in the NICMOS images. However, the mismatch is small enough to avoid any ambiguities in identifying a source in the various bands.

The transformations between the coordinates of the FOC UV images of these galaxies and the WFPC2 images were similarly calculated, and the UV sources tabulated by Maoz et al. (1996) matched with their optical counterparts. To produce an image of the  $(\text{H}\alpha + [\text{N II}])/\text{Pa}\alpha$  ratio, we first matched the angular resolution of the  $\text{H}\alpha + [\text{N II}]$  image and the  $\text{Pa}\alpha$  image by convolving each image with the PSF of the other image’s bandpass. The WFPC2 F658N and NICMOS2 F187N PSFs were determined using the Tiny Tim software (Krist & Hook 1997). We then subtracted a median background level from each continuum-subtracted, smoothed, emission-line image, and divided the two.

Figures 1 and 2 show mosaics of the final galaxy images in the different observed bands. Figures 3 and 4 show several color-composite views of each galaxy, combining data from several bands. Figures 5 and 6 illustrate the  $(\text{H}\alpha + [\text{N II}])$  and  $\text{Pa}\alpha$  images with the main line-emission complexes marked. Figures 7 and 8 show the  $\text{H}\alpha + [\text{N II}]$  emission as contour plots superimposed on the “ $U$ -band” F336W images. Figure 9 gives the  $(\text{H}\alpha + [\text{N II}])/\text{Pa}\alpha$  ratio map for NGC 1512. The large width of the ring in NGC 5248 (see below) results in a low emission-line surface brightness and a noisy  $(\text{H}\alpha + [\text{N II}])/\text{Pa}\alpha$  ratio map of limited utility, which we therefore do not show.

### 3. Analysis

#### 3.1. Ring Morphology

Although similar in most respects (see below), the overall morphologies of the circumnuclear rings differ in NGC 1512 and NGC 5248. NGC 1512 has a highly ordered and narrow ring, with a radius-to-width ratio of  $\sim 10$ . Nearly all of the line emission and the compact sources are concentrated in this ring. In NGC 5248, the radius-to-width ratio



is  $\sim 2$ , and the H II regions are distributed over a much larger area. These differences may be related to the fact that NGC 1512 is a more strongly barred galaxy than NGC 5248. NGC 5248 also has a second, inner, ring of  $2.5''$ -diameter major axis (120 pc, assuming a distance of 10 Mpc), which is seen most clearly in its  $H\alpha + [N II]$  image. To our knowledge, this feature has not been noted as such before, but it coincides with the inner part of the spiral found in continuum images by Laine et al. (1998).

Comparison of the images of each galaxy in the various filters reveals a number of features. The appearance of the galaxies changes dramatically when going from the UV to the IR, because of the growing prominence of the red populations of the central galactic regions. At first glance, the appearance of the circumnuclear rings does not seem to change so drastically between bands, with the same major complexes of star formation being traceable from the UV to the IR. Closer examination shows, however, that the structure within individual complexes is strongly wavelength dependent. Specifically, the individual stars and clusters have a large range in color, making the most prominent sources in one band inconspicuous or absent in another band. A good example of this is the close pair of bright clusters in the southeast part of the NGC 1512 rings (top of panel in Figure 1.) The lower-left member of the pair is considerably fainter in the UV bands, but is brighter than the upper-right cluster at  $1.6 \mu m$  (see also §3.3.5). Similarly, a progressively larger number of sources become discernible as one goes to the IR, and their IR fluxes are comparable to the IR fluxes of the bright UV sources. This large diversity in color and in the bands in which specific sources are above the detection threshold create the “Christmas tree” appearance of the color composites in Figures 3 and 4. This phenomenon is treated more quantitatively and physically in §3.3.

The UV images of the galaxies show that the brightest regions follow a definite spiral, rather than ring, structure. The optical and IR images prove, however, that this effect is produced by spiral dust structures that cross the rings. As dust obscuration becomes less pronounced at IR wavelengths, the “gaps” between the ends of the spirals nearly close. The true ring morphology of the underlying ionizing population is seen clearly in the  $H\alpha + [N II]$  and  $Pa\alpha$  images, in which the spiral structure is no longer evident.

### 3.2. Continuum and Line Emission, and Extinction

The continuum and emission-line images differ in appearance not only in terms of the spiral structure, but in other respects as well. While the brightest continuum emission from the circumnuclear rings comes from numerous compact (see below) clusters and stars, the  $H\alpha + [N II]$  and  $Pa\alpha$  emission occurs in more extended, resolved clumps encompassing

entire complexes of clusters. In several regions, the line-emitting gas may actually have a bubble morphology, surrounding a group of young clusters. In the parts of the rings showing both strong continuum and line emission (e.g., the bright southern complex in NGC 1512 – top of Figure 7), closer examination of the  $H\alpha$ + $[N\ II]$  contour map overlaid on the  $U$ -band continuum image shows that the brightest emission-line clumps are at positions that are offset from the brightest continuum sources. This suggests that expansion due to winds or ionization fronts around the clusters clears out the gas and the dust. Such shell-like or bubble-like morphologies around young clusters are also seen, for example, in NGC 1569 (Hunter et al. 2000), NGC 5253 (Strickland & Stevens 1999), and NGC 4214 (Maíz-Apellániz et al. 1999).

More remarkably, perhaps (and as already noted above), in some regions of the rings the line emission and continuum emission are mutually exclusive. This is conspicuous, for example, in NGC 5248 (Figure 8), where clumps of  $H\alpha$ + $[N\ II]$  emission trace ionizing sources that are not detected in any of the continuum bands. This type of emission-line/continuum avoidance has been noted before in other starbursts (e.g., Ravindranath & Prabhu 1998; Buta et al. 2000). It can be seen clearly, for instance, in the *HST* composite  $H\alpha$  and continuum image of the merging galaxy pair NGC 4038/4039 (Fig. 4 in Whitmore et al. 1999).

To investigate this phenomenon quantitatively, we have measured the emission-line and continuum fluxes from the main H II complexes along the rings. Table 2 lists the integrated  $H\alpha$ + $[N\ II]$ ,  $P\alpha$ , and  $1.6\ \mu\text{m}$  fluxes, and their ratios, as measured in circular apertures roughly centered on the main emission-line complexes. The labels and apertures for each complex are marked in Figures 5 and 6. The radii of the apertures, also listed in Table 2, were approximately matched to the size of each emission complex. Because of the spatial correlation between the H II regions, the definition of what constitutes an individual region is not unique, and the choices of regions and radii are somewhat subjective. These measurements nevertheless provide some rough estimates of the physical properties of the gas. Quillen & Yukita (2000) have compiled a similar table for NGC 1512. Apart from the incorrect calibrations, mentioned above, there seems to be an error in the offset coordinates of some of the H II regions they list (e.g., the bright complexes 4, 5, 7, and 8 are not on their list).

Assuming approximate distances of 10 Mpc to the galaxies, the typical diameters of the brightest H II regions are in the range 20-50 pc, and the observed  $H\alpha$ + $[N\ II]$  luminosities are  $10^{37}$  to  $10^{38}$  erg s $^{-1}$ . As we will see below, based on the  $P\alpha/H\alpha$  intensity ratios, the typical extinction of  $H\alpha$  is 1–2 mag, or more, if the gas and dust are mixed, as seems to be the case. The extinction-corrected  $H\alpha$ + $[N\ II]$  luminosities are therefore about an order of

magnitude higher than the above numbers. For comparison, the  $H\alpha$  luminosity of the Orion nebula is  $10^{37}$  erg s $^{-1}$ , and that of 30 Doradus is about  $3 \times 10^{39}$  erg s $^{-1}$ , the rough lower limit denoting “giant H II regions” (Kennicutt & Chu 1988). The total  $H\alpha + [N II]$  luminosities of the rings, obtained by integrating the fluxes over the entire rings, are  $6 \times 10^{39}$  erg s $^{-1}$  (NGC 1512) and  $9 \times 10^{39}$  erg s $^{-1}$  (NGC 5248). Again, the extinction-corrected luminosities are likely an order of magnitude larger, or about  $10^{41}$  erg s $^{-1}$ . This is very similar to the  $H\alpha$  luminosity derived by Buta et al. (2000) for the starburst ring in NGC 1326. It implies an ionizing photon luminosity of  $7 \times 10^{52}$  s $^{-1}$  and a star-formation rate of about  $1 M_{\odot}$  yr $^{-1}$ , assuming a continuous starburst with a Salpeter initial mass function (IMF) from 0.1 to  $100 M_{\odot}$  (Kennicutt 1998).

The  $Pa\alpha/f_{\lambda}(1.6 \mu m)$  ratio, or the equivalent width of  $Pa\alpha$ , is a good age indicator, since it basically measures the ratio of O stars to K and M giants and supergiants, and is insensitive to reddening because both measurements are at similar wavelengths. Using spectral synthesis models (see §3.3.3 for details) for a starburst with a star-formation rate that exponentially decays on a timescale of 1 Myr, we find that the  $Pa\alpha/f_{\lambda}(1.6 \mu m)$  ratio has a value of  $\sim 400 \text{ \AA}$  for the first few  $10^6$  yrs. It then declines by 2 orders of magnitude and becomes of order  $1 \text{ \AA}$  by  $\sim 10^7$  years. The nebular continuum emitted by the gas is included in this calculation.

The observed ratios in Table 2 are actually lower limits to the intrinsic ratios for the starbursts producing the lines, because our integration includes continuum emission from unrelated foreground and background populations of stars. From the observed numbers, which are roughly in the range 50–500  $\text{\AA}$ , we see that the bright emission-line complexes have the ratios expected for a mixture of gas and an ionizing population that is a few million years old.

The  $(H\alpha + [N II])/Pa\alpha$  ratios, also listed in Table 2, can give some indication of the amount of dust mixed with, or along the line of sight to, the gas. As explained in more detail below, in the absence of reddening, the expected  $(H\alpha + [N II])/Pa\alpha$  ratio in these galaxies is about 10. The ratios listed in Table 2 are typically 2 to 5 times lower, and thus indicate some extinction in most of the complexes. The  $(H\alpha + [N II])/Pa\alpha$  ratio map of NGC 1512 in Figure 9 reveals additional interesting information regarding the line emission. The overlaid contours are the  $Pa\alpha$  emission, marking the regions where there is significant detected flux in this line, above a level of  $7.7 \times 10^{-16}$  erg s $^{-1}$  cm $^{-2}$  arcsec $^{-2}$ . The inner contour corresponds to  $20 \times 10^{-16}$  erg s $^{-1}$  cm $^{-2}$  arcsec $^{-2}$ . The  $Pa\alpha$  image is shallower than the  $H\alpha + [N II]$  image, because of the lower flux in  $Pa\alpha$ , and the lower sensitivity, higher background, and poorer angular resolution in the IR. The  $Pa\alpha$  image therefore limits the regions where the ratio can be measured reliably; outside the outer marked contours, the

ratio is dominated by noise and background residuals. The whitest regions correspond to a ratio of about 1, while the darkest areas have a ratio of  $\sim 10$ . Concentrating on the pixels within the contours of significant  $\text{Pa}\alpha$  emission, we see that most of these have a greyish shade, which corresponds to ratios of about 4. The same is true for NGC 5248 (ratio map not shown), but the low surface brightness of  $\text{Pa}\alpha$  in that galaxy limits the measurement to a few small regions.

The dominant error in the ratio is caused by the uncertainty in the background levels that need to be subtracted from the  $\text{H}\alpha + [\text{N II}]$  and  $\text{Pa}\alpha$  images prior to their division. To estimate this error, we created ratio images using extreme plausible values for the backgrounds. We find that, within the marked  $\text{Pa}\alpha$  contours, the  $(\text{H}\alpha + [\text{N II}])/\text{Pa}\alpha$  uncertainty is  $\sim \pm 20\%$ , decreasing to  $\pm 5\%$  in the regions of highest line emission. This error is compounded by the  $\pm 15\%$   $\text{Pa}\alpha$  calibration uncertainty in NGC 5248 due to the unknown line-of-sight velocity of each clump.

The expected Case B recombination value of  $\text{H}\alpha/\text{Pa}\alpha$  is about 8.5. The heliocentric radial velocities of these galaxies ( $911 \text{ km s}^{-1}$  for NGC 1512, and  $1156 \text{ km s}^{-1}$  for NGC 5248) places both lines of the  $[\text{N II}] \lambda\lambda 6548, 6583$  doublet also within the F658N bandpass. For the nucleus of NGC 1512,  $[\text{N II}] \lambda 6548$  is on the blue edge of the bandpass, at about 10% of the peak transmission, while  $[\text{N II}] \lambda 6583$  falls on the flat transmission plateau, along with  $\text{H}\alpha$ . For NGC 5248, the  $[\text{N II}]$  lines are on the rising and falling parts of the bandpass, each at about 50% of the peak transmission, and  $\text{H}\alpha$  is on the plateau. However, the individual H II regions in the rotating rings can have line-of-sight velocities of order  $100 \text{ km s}^{-1}$  relative to that of the nucleus (e.g., Maoz et al. 1996), shifting the lines by  $\sim \pm 2 \text{ \AA}$ , and changing somewhat the relative contributions of each of the  $[\text{N II}]$  lines to the counts in the bandpass. The nuclear spectrum of NGC 5248 presented in Ho, Filippenko, & Sargent (1995) shows the  $[\text{N II}]$  lines to be of comparable strength to  $\text{H}\alpha$ . However, in the circumnuclear H II regions, the  $[\text{N II}]$  lines, relative to  $\text{H}\alpha$ , are usually much weaker (e.g., Ho, Filippenko, & Sargent 1997). Specifically, we have measured the relative line strengths of  $[\text{N II}]$  and  $\text{H}\alpha$  in two of the ring H II regions that fall along the slit in the Ho et al. (1995) spectrum of NGC 5248. Assuming these two H II regions are representative of the rest, and accounting for the F658N transmission at the systemic velocity,  $[\text{N II}]$  contributes 14% to 18% of the counts in the bandpass. The maximum  $[\text{N II}]$  contamination,  $\sim 23\%$  to  $28\%$ , will be for a velocity of  $-100 \text{ km s}^{-1}$  relative to systemic. We do not have a spectrum of NGC 1512, but assuming it is similar to NGC 5248, at the systemic velocity  $[\text{N II}]$  contributes 22% to 28% to the counts, and less than this for velocities of order  $\pm 100 \text{ km s}^{-1}$ . From all these considerations, in the absence of reddening, we expect the observed  $(\text{H}\alpha + [\text{N II}])/\text{Pa}\alpha$  flux ratio in both galaxies to be in the range of 10 to 12, substantially above the  $\text{H}\alpha/\text{Pa}\alpha$  ratio.

The typical values integrated over complexes (Table 2) and observed in the ratio maps, in the range of 2–5, again suggest that the line-emitting gas suffers from some dust extinction. Assuming the Galactic extinction curve of Cardelli, Clayton, & Mathis (1989), with  $A_V = 3.1E(B - V)$ , a moderate amount of extinction,  $A_V \approx 1.5\text{--}3$  mag, by a foreground dust screen would produce the observed values. Alternatively, the gas and dust may be mixed. The observed line ratio is then just the intrinsic ratio times the ratio of the optical depths. For an infinite gas+dust slab ( $\tau \gg 1$ ) the expected line ratio is about 2, similar to what is seen in many of the regions. It is likely that a combination of these two geometries is operating in practice. This would explain the absence of continuum sources associated with some of the main emission-line complexes.

Examining in closer detail the ratio maps, they do reveal some small, dark-coded clumps, often near the peaks of line emission, corresponding to higher  $(\text{H}\alpha + [\text{N II}])/\text{Pa}\alpha$  ratios, of about 6 to 9. These must be regions where the gas either undergoes less extinction, or has a lower ionization spectrum, with a higher  $[\text{N II}]/\text{H}\alpha$  ratio, more similar to that of the nucleus. This can arise through excitation by shocks, or photoionization by unusually hot stars, which produce a hard ionizing continuum (Shields & Kennicutt 1995; Ho et al. 1997). Similarly, some regions of the rings also have lower  $(\text{H}\alpha + [\text{N II}])/\text{Pa}\alpha$  ratios. For example, patch No. 6 in the west side of the ring in NGC 1512 has a fairly uniform value of  $(\text{H}\alpha + [\text{N II}])/\text{Pa}\alpha \approx 1\text{--}2$ . The small ratio in this patch can also be appreciated by examining directly the  $\text{H}\alpha + [\text{N II}]$  and  $\text{Pa}\alpha$  images in Figure 5. In NGC 1512, we do not see any regions that have detected  $\text{Pa}\alpha$  emission, but little or no  $\text{H}\alpha + [\text{N II}]$ . NGC 5248, on the other hand, does have some  $\text{Pa}\alpha$  clumps that are faint or undetected in  $\text{H}\alpha + [\text{N II}]$  (for example clumps No. 15 and 16). The average  $(\text{H}\alpha + [\text{N II}])/\text{Pa}\alpha$  in these clumps is  $\lesssim 1$ , with lower values in particular regions of a clump. This indicates foreground dust, equivalent to the effect of  $A_V \approx 3\text{--}4$  mag of Galactic dust, along the line of sight to some of the line-emitting gas in this galaxy.

We find additional evidence for substantial dust extinction by comparing the rings’ total ionizing photon luminosities of  $7 \times 10^{52} \text{ s}^{-1}$ , derived above based on the  $\text{H}\alpha$  flux, to their UV luminosities. Maoz et al. (1996) measured total flux densities at  $2300 \text{ \AA}$  for each of the rings, of  $f_\lambda = 8.5 \times 10^{-15} \text{ erg s}^{-1} \text{ cm}^{-2} \text{ \AA}^{-1}$ , or specific luminosities  $L_{2300} = 10^{38} \text{ erg s}^{-1} \text{ \AA}^{-1}$  at the assumed 10 Mpc distances. They found that  $\sim 40\%$  of this total UV flux comes from compact sources, and mostly from the few brightest ones. As we will see below (§3.3.4), the SEDs of these bright clusters are like those expected from clusters that are 1–10 Myr old undergoing typical attenuations at  $2300 \text{ \AA}$  by factors of 4 (in NGC 1512) to 18 (in NGC 5248). The extinction-corrected luminosities are therefore  $L_{2300} = 4 \times 10^{38} \text{ erg s}^{-1} \text{ \AA}^{-1}$  (NGC 1512) and  $L_{2300} = 2 \times 10^{39} \text{ erg s}^{-1} \text{ \AA}^{-1}$  (NGC 5248).

From our spectral synthesis models, we find that a 1 Myr-old starburst with the above UV luminosities produces  $(6 - 30) \times 10^{52} \text{ s}^{-1}$  ionizing photons, while a 10 Myr-old model with the same UV luminosity produces fewer ionizing photons by two orders of magnitude. Thus, under the extreme assumption that all the observed UV light is produced by a stellar population that is only 1 Myr old (or, equivalently, all the UV light is produced predominantly by O-type stars), the deduced ionizing photon flux is similar to that implied by the extinction-corrected  $\text{H}\alpha$  flux. For a more conservative assumption about the spectrum of the integrated ionizing population, there is a deficit of ionizing photons by a factor of 1–100. This again indicates that the blue sources we see are only a fraction of the ionizing sources, while some are inside the line-emitting gas, and extinguished by the dust mixed with it. Given the uncertainties in determining the emission-line extinction and the precise ages of the ionizing sources, it is difficult to say what the exact obscured fraction is.

A peculiar, compact, emission-line source is found in the northern side of the ring in NGC 1512 [PC position (452,251), NICMOS position (204,194), labeled “A” in Fig. 5]. In the  $\text{H}\alpha + [\text{N II}]$  image it is one of the highest surface-brightness objects, but is very compact and round, with a FWHM of  $0.1''$ , and total  $\text{H}\alpha + [\text{N II}]$  flux of  $2 \times 10^{-15} \text{ erg s}^{-1} \text{ cm}^{-2}$ , or an  $\text{H}\alpha + [\text{N II}]$  luminosity of  $2.4 \times 10^{37} \text{ erg s}^{-1}$ . In the  $\text{Pa}\alpha$  image, it is barely detected, and we estimate the  $(\text{H}\alpha + [\text{N II}]) / \text{Pa}\alpha$  ratio to be  $\sim 25$ . In the broad bands, this source is detected, if at all, as a faint, unresolved object. It is undetected in the UV in the FOC/F220W, with a limit of  $f_\lambda(2300 \text{ \AA}) < 30 \times 10^{-19} \text{ erg s}^{-1} \text{ cm}^{-2} \text{ \AA}^{-1}$ , but detected with WFPC2 in F336W, with  $f_\lambda(3350 \text{ \AA}) = (7 \pm 2) \times 10^{-19} \text{ erg s}^{-1} \text{ cm}^{-2} \text{ \AA}^{-1}$ . It is only barely detected in the F547M band, with  $f_\lambda(5490 \text{ \AA}) \approx (1.5 \pm 1) \times 10^{-19} \text{ erg s}^{-1} \text{ cm}^{-2} \text{ \AA}^{-1}$ , i.e.,  $V \approx 26 \text{ mag}$ , or  $M_V \approx -4$ . At longer wavelengths, in the WFPC2 F814W and NICMOS F187W bands, it brightens again, with  $f_\lambda(8040 \text{ \AA}) = (5 \pm 2) \times 10^{-19} \text{ erg s}^{-1} \text{ cm}^{-2} \text{ \AA}^{-1}$ , and  $f_\lambda(1.6 \text{ }\mu\text{m}) = (4.5 \pm 1.5) \times 10^{-19} \text{ erg s}^{-1} \text{ cm}^{-2} \text{ \AA}^{-1}$ . Given the large equivalent width of  $\text{H}\alpha + [\text{N II}]$  (about  $7000 \text{ \AA}$ ), it is possible that the counts in the broad bands are affected or dominated by other emission lines.

In view of the discussion above, if the object has a recombination spectrum, then most of the flux in the  $\text{H}\alpha + [\text{N II}]$  band will be  $[\text{N II}]\lambda 6583$ , with a ratio of  $[\text{N II}]\lambda 6583 / \text{H}\alpha$  of about 2, or more if the line emission is reddened. Alternatively, other types of line excitation may be at work. The properties of this source are similar to those of “Balmer-dominated” supernova remnants (SNRs) that are seen in the Galaxy (e.g., Tycho’s SNR) and in the Large Magellanic Cloud (LMC; Smith et al. 1991). The optical light from these young (typically  $< 1000 \text{ yr}$ ) SNRs consists almost exclusively of  $\text{H}\alpha$ , which is thought to arise from a very fast shock that excites the line through collisional excitation of neutral hydrogen atoms and charge transfer with protons. Object A may be the first Balmer-dominated SNR found beyond the LMC. Another possibility is that object A is a supernova event similar to

SN 1986J (Rupen et al. 1987; Leibundgut et al. 1991) and SN 1988Z (Aretxaga et al. 1999, and references therein). These objects last a long time, and have late-time optical spectra totally dominated by  $H\alpha$  emission.

### 3.3. Compact Sources

#### 3.3.1. Source Selection

A primary goal of our work is to improve our understanding of the numerous discrete sources – compact clusters and individual stars – that appear in the circumnuclear rings, by measuring their SEDs. As seen in the figures above, the prominence of individual sources can change dramatically, with some that are bright in one band becoming faint or undetected in another. We wish to obtain fluxes, or upper limits on fluxes, in every band for every source that appears in one or more bands.

We therefore created a summed “UV-optical” image consisting of the F220W, F336W, F547M, and F814W images, which were first scaled to all have similar means. The DAOFIND task was applied to this combined image to create a list of discrete sources. The complicated, uneven background and crowding of the sources mandated that the output of this task be edited manually, to delete false detections and append obvious misses. Such a procedure was found to be unavoidable also in previous work on these and other ring galaxies (Barth et al. 1995; Maoz et al. 1996). We verified that no obvious sources appearing in the individual optical-UV bands had been overlooked. We attempted to locate all sources in the regions of the rings, but not in the more exterior regions, which are outside the fields of view of the FOC and NICMOS, nor interior to the rings, where the bright stellar background makes it progressively more difficult to detect sources at smaller radii and at longer wavelengths. This procedure cannot be considered objective, but our compilation should be complete for the brightest sources in each ring. In any event, there are few clusters outside or inside the rings. Altogether, 325 optical-UV sources were selected in NGC 1512 and 397 in NGC 5248.

Most of the sources in the NICMOS  $1.6\ \mu\text{m}$  exposures are not obviously detected in the optical images. We therefore applied the same source detection procedure separately to the F160W images. Of the 221 IR sources in NGC 1512, 150 were not selected in the UV-optical image. In NGC 5248, 110 of the 191 IR sources were not selected in the UV-optical image. The combined UV-optical-IR lists of sources thus consist of 475 sources in NGC 1512 and 507 sources in NGC 5248.

### 3.3.2. Photometry

Aperture photometry at the positions of the sources in the final list was carried out on the images in each individual band using the PHOT task in IRAF. For the WFPC2 images, apertures of radii 1, 2, and 3 pixels were used. The 2-pixel-radius apertures are best suited for WFPC2 PC photometry, since they are large enough to minimize photometry errors due to pixelation and to centering errors, but small enough to minimize the effects of crowding on the photometry (e.g., Barth et al. 1995). The NICMOS images have a larger PSF and a coarser pixel scale, with one NICMOS pixel corresponding to about 1.67 PC pixels. To avoid uncertainties in the photometry due to the resampling and registration of the NICMOS images, NICMOS photometry was performed on the original images. The positions on the NICMOS frames of all the UV-through-IR-selected sources were computed, based on the geometric transformations described above. We used an aperture of radius 1.79 NICMOS pixels, which is equivalent in angular scale to 3 WFPC2 PC pixels. This was chosen as a compromise, given the constraints, on the one hand, to match approximately the PC apertures in order to measure the same objects in the optical and IR bands and avoid crowding effects while, on the other hand, to avoid overly small apertures that will be susceptible to pixelation and centering errors.

Aperture corrections need to be applied to the measurements to account for the fact that not all the light of the PSF is included within the aperture. As discussed in §3.3.7, the individual sources in these galaxies appear to be unresolved or marginally resolved. We therefore calculated the aperture corrections by generating artificial PSFs for each of the WFPC2 and NICMOS bands using the Tiny Tim software, and finding the ratio between counts within the radii used for the photometry and the radii corresponding to  $1.4''$ , which should include 99% of the light according to the STScI website.

Photometry errors due to photon statistics and background uncertainties were calculated by the PHOT task. To this, we added in quadrature a calibration uncertainty of 5%, which includes the effects of flat-fielding errors, charge-transfer efficiency and UV contamination variations in the WFPC2 detectors, uncertainties in aperture corrections, and uncertainties in the absolute sensitivities of each of the bands (see the WFPC2 and NICMOS Data Handbooks).

After aperture correction and photometric calibration, all of the photometry was consolidated into one list for each galaxy, including the 2300 Å fluxes from Maoz et al. (1996). Tables 3 and 4 show the final photometry ordered by brightness in the F547M filter, in decreasing order, for each of the galaxies. The full tables for all the measured sources in both galaxies are available in the electronic version of the journal.



Figure 10 is a color-magnitude diagram showing, for both galaxies, all of the sources detected in F547M and F814W. For ease of comparison with other work, the data in this figure have been converted to standard  $V$  and  $I$  magnitudes according to the transformations of Holtzman et al. (1995). The  $V$  magnitudes also appear in Tables 3 and 4. The figure shows that the brightest sources are blue, with  $V - I \approx 0$ . The sources in NGC 5248 have a larger spread in color than those in NGC 1512, and are typically 0.5-1 mag redder.

Figures 11–12 plot the SEDs of the brightest individual sources in each galaxy. For clarity, only the 25 brightest sources in each galaxy are shown, separated into different panels according to brightness in  $V$ , and error bars are omitted. Missing measurements at 2300 Å and at 1.6  $\mu\text{m}$  are for objects outside the field of view of the FOC or NICMOS, or, for the fainter objects, are below the detection limits.

A cursory examination of the SEDs again shows that almost all of the bright sources are blue, with spectra that can be approximated as  $f_\lambda \propto \lambda^\beta$ , with slopes  $\beta$  of  $-1$  to  $-3$ . These sources apparently undergo little reddening. There are no bright sources that have SEDs which rise to the red. The most luminous known red supergiants have  $M_V \approx -7$  mag, or, at 10 Mpc,  $V \approx 23$  mag and  $f_\lambda(5490 \text{ Å}) \approx 2 \times 10^{-18} \text{ erg s}^{-1} \text{ cm}^{-2} \text{ Å}^{-1}$ . While many of the sources in the rings, including some of the more luminous ones, are only a few times brighter than this, their blueness excludes the possibility that they are individual red supergiants, rather than young clusters. As for individual blue supergiants, they can have even higher luminosities, up to  $M_V = -10$  mag, but they are extremely short-lived and rare, and hence are not plausible candidates for explaining any but a handful of the observed sources. If, for the purpose of a rough appraisal of the content of the clusters, one assumes the UV is dominated by the light of main-sequence B0 stars, the observed fluxes (uncorrected for extinction) of the 25 brightest clusters correspond to 5 to 500 such stars. For reasonable IMFs, the total masses of these clusters are of order  $10^4$  to  $10^6 M_\odot$ . Masses in this range also result from our detailed model fitting (§3.3.6).

It is only the sources with  $f_\lambda(5490 \text{ Å}) \lesssim 2 \times 10^{-18} \text{ erg s}^{-1}$  that may, indeed, often be individual supergiant stars. However, some of these objects may also be reddened SSCs and old, or low-mass, clusters. For reference, old globular clusters have  $M_V \approx -7$  mag, similar to the most luminous red supergiants. Thus, some of the faint objects could also be old globulars from a previous starburst. This possibility is examined in more detail below.

### 3.3.3. Cluster Models

To interpret the measured SEDs, we use the population and spectral synthesis code STARS (Sternberg 1998; Thornley et al. 2000) to generate model SEDs of clusters with a range of ages and assumed foreground extinctions. For the population synthesis, STARS employs the Geneva stellar evolutionary tracks (Schaller et al. 1992). In the computations presented here, we assume solar metallicity tracks. We also assume a time-independent power-law IMF,  $dn/dm \propto m^{-\alpha}$ , between a lower and an upper mass limit. For the spectral synthesis of the cluster SEDs we adopt the procedures described in Thornley et al (2000). Briefly, the spectral energy distributions (SEDs) for individual stars are taken from a “hybrid grid” generated from two libraries of theoretical model atmospheres. For stars with effective temperatures  $< 19000$  K we use the Kurucz (1992) models which assume atmospheres in local thermodynamic equilibrium (LTE). For hotter stars ( $25000 - 65000$  K) we adopt the more realistic non-LTE models of Pauldrach et al. (1998). The SEDs for intermediate temperatures are obtained by interpolation between the Kurucz and the Pauldrach et al. models. A more detailed discussion and comparison of the library SEDs is presented in Thornley et al. (2000).

We have compared some of our broad-band photometric computations with those of other codes, such as STARBURST99 (Leitherer et al. 1999), and find good agreement. For example, our computed  $V$  magnitudes agree well (generally to within 0.3 mag) with those of Leitherer et al. for both continuous and decaying bursts and a range of IMF slopes and upper mass cutoffs.

Within the scope of the present study, we have limited ourselves to models with a Salpeter (1955) IMF with upper and lower mass limits  $M_{up} = 120M_{\odot}$  and  $M_{low} = 1M_{\odot}$ , solar metallicity, and an exponentially decaying star-formation rate with a characteristic timescale of 1 Myr. Solar metallicity is a reasonable assumption for circumnuclear regions of barred spirals, where radial mixing occurs (e.g., Roy & Belley 1993; Martin & Belley 1997), and, in any event, the broad-band properties are weakly dependent on metallicity (e.g., Leitherer & Heckman 1995). We find that the model calculations are only weakly affected if, instead of a Salpeter slope of  $-2.35$  we assume an IMF slope of  $-2.5$ , or if the burst timescale is 5 Myr instead of 1 Myr. Figure 13 illustrates the spectral evolution of a model cluster. The five curves correspond to ages of 1, 10, 30, 100, and 300 Myr, with the steepest SED corresponding to the youngest age, and then fading with age. An arbitrary vertical shift has been applied to the models as a whole (but not relative to each other). A vertical shift is equivalent to a change in the mass of a cluster or in the distance to a galaxy.

The light from a 1 Myr-old model cluster is dominated at all bands by main-sequence O and B stars, and by evolved massive stars. The overall spectral slope is approximately a

power law with slope  $\beta \approx -3.5$ . By 10 Myr, the SED develops a change of slope longward of the Balmer edge, where the light becomes dominated by red supergiants, but the slope at shorter wavelengths also flattens, as the most massive stars disappear. The continued evolution of the cluster is characterized mainly by a slow overall fading, along with a strengthening of the Balmer jump, and only mild changes of slope. Note that there is less than a factor of 10 difference in  $V$  luminosity between the oldest and youngest model clusters we have considered. Therefore, coexisting clusters within this wide range of ages can be detected, in principle. As we show below, however, the steep mass and luminosity functions of the clusters create an age bias that will cause young clusters to appear highly over-represented in a given sample.

Figure 14 illustrates the effects of extinction by foreground dust on one of the models, and was calculated using the Galactic extinction curve of Cardelli et al. (1989), with  $A_V = 3.1E(B - V)$ . Although many other extinction laws are possible, we will, again, limit our investigation to this one.

#### 3.3.4. Color-Color Diagrams

One way of comparing the models and the observations is by means of color-color diagrams, as has been done, for example, by Whitmore et al. (1999) and Buta et al. (2000). A problem with this method is that, for particular choices of bands, the age trajectories of model clusters sometimes “backtrack” on themselves, making it difficult to uniquely determine the ages of some of the observed clusters. Furthermore, age and extinction may move points in the diagram in a similar direction, so that there is a degeneracy in these two parameters. We have found that most of the color-color plots we can make with our available broad-band data suffer from the same problems. However, the use of the UV (2300 Å) band can partly solve this. Figure 15 shows the models and the data on a plot of  $2.5 \log[f(2300 \text{ Å})/f(3350 \text{ Å})]$  vs.  $2.5 \log[f(3350 \text{ Å})/f(5490 \text{ Å})]$  (essentially,  $U - UV$  and  $V - U$ , up to additive constants). The model fluxes were calculated by integrating the model SEDs over a bandwidth equal to the filters’ FWHM. Cluster aging trajectories for several values of foreground extinction are shown. Ages, in Myr, are marked in large numerals along the top trajectory. One sees that, in this color-color space, the individual trajectories are well stretched out, partly solving the “backtrack” problem. The reddening shifts the curves in a direction nearly orthogonal to the aging direction, partly alleviating the age-extinction degeneracy. Unfortunately, it is possible to place on this plot only the  $\sim 40$  clusters in each galaxy that were detected in the relatively shallow pre-refurbishment FOC UV images. Nevertheless, these plots are revealing.

Figure 15 plots with progressively smaller symbols sources that are fainter in  $V$ . Typical error bars are shown in the corner. To avoid cluttering, only the brightest clusters are labeled according to their designations in Tables 3 and 4. It is clear that the brightest clusters are very young, with ages generally less than 5 Myr for the 15 brightest clusters, and generally less than 10 Myr for all the UV-detected clusters. Furthermore, the extinctions are quite moderate, with the brightest sources clustered around visual extinctions of  $A_V = 0.5$  mag in NGC 1512 and  $A_V = 1$  mag in NGC 5248. These correspond to the attenuations at 2300 Å by factors of 4 and 18, respectively, already mentioned in §3.2.

To illustrate the form of a color-color diagram in another band, for which most of the sources do have measurements, Figure 16 plots the same model trajectories in the plane of  $2.5 \log[f(3350 \text{ Å})/f(5490 \text{ Å})]$  vs.  $2.5 \log[f(5490 \text{ Å})/f(8040 \text{ Å})]$  (essentially,  $V - U$  and  $I - V$ , up to additive constants). For clarity, only the models are shown in this plot. The problems of backtracking and age-extinction degeneracy are evident. In Figure 17, the data for NGC 1512 are added to a similar plot, which shows additional extinctions, but omits some age labels and all cluster labels for clarity. The 20 clusters brightest in  $V$  are again shown as the largest points, and each set of the next 100 brightest sources is plotted with progressively smaller dots. Most of the clusters have separations from at least some model trajectories that are consistent with the statistical and systematic calibration uncertainties of the measurements, as represented by the typical error bars plotted. As in Figure 15, the diagram indicates that most of the bright clusters are young and only mildly reddened. However there are two bright sources above, and to the left of, the others, that are simultaneously very blue in  $V - U$ , but red in  $I - V$ , and are about 0.5 mag from the nearest model. (These are sources Nos. 7 and 17 in Table 3.) This “IR-excess” phenomenon is examined in more detail below. For most of the fainter sources, it is impossible to disentangle age and extinction in this plot, and the larger measurement errors exacerbate the problem. Some of the faintest sources are probably individual stars.

### 3.3.5. *Model Fitting – Cluster Ages and Extinctions*

Another method of estimating ages and extinctions, which exploits all the available broad-band information, is to directly compare the modeled and observed SEDs. To this end, we have generated a grid of models with ages between 1 Myr and 300 Myr, and extinctions between 0 and  $A_V = 3$  mag. Each model SED was multiplicatively scaled to best match each observed SED and the  $\chi^2$  residual of the fit calculated. Figure 18 shows examples of three observed SEDs in NGC 5248 and their model fits. For the fainter cluster displayed, two models are illustrated — one that fits well, and one that is marginally

consistent with the data. This demonstrates the power of this diagnostic technique when measurements in numerous bands over a wide wavelength range are available. For most of the observed SEDs we can find at least one model that provides an acceptable fit. Given the observational uncertainties in the SEDs and the remaining age-extinction degeneracy in some cases (e.g., for some clusters without a UV measurement), more than one model can fit most of the observed sources.

However, some sources are poorly fit by all models we have considered. Surprisingly, it is the brightest (and bluest) sources in both galaxies that often suffer from this problem, even though these are least susceptible to measurement errors due to, e.g., crowding and background uncertainties. Figure 19 shows examples of SEDs and best-fit models for four such clusters in NGC 1512 (Nos. 2, 3, 4, and 8 in Table 3). Clearly, the poor fit of the models (which are all formally rejected) is due to the  $1.6 \mu\text{m}$  measurements, which are 2-5 times higher than the predictions of the models that reproduce well the data in the other bands.

It is unlikely that this IR deviation in some of the bright sources is a calibration problem, since most of the sources in both galaxies *are* well fit in all bands, including the IR. The phenomenon can actually be seen directly by examining, in Fig. 1, the two close bright clusters near the 12 o'clock position. These are clusters Nos. 1 and 5 in Table 3 (i.e. the brightest, and fifth brightest, in  $V$ ), and their SEDs appear in Fig. 11. Cluster No. 1 is several times brighter than cluster No. 5 in all bands, except in the IR, where clearly No. 5 overpowers No. 1. Cluster No. 1 is about as blue as a cluster can be, so if one changed the IR calibration to make the SED of No. 5 fit the models, cluster No. 1 (and many others, too) would be too blue (i.e., too weak in the IR) to fit any model. This, again, argues against a calibration problem. One could invoke a systematic error, such as saturation, that affects only the brighter sources. However, saturation would make bright sources appear anomalously faint, rather than bright, and, in any case, no such effect has been reported with NICMOS for sources of this brightness.

We believe that the observed IR excess is real, and signals some physical element that is absent from the models. As an example, the dashed line in Figure 19 shows the effect of adding to the lower model a 2000 K blackbody, scaled to reproduce the IR excess of the fainter cluster in the diagram. The excess in this object is large enough that it seems to appear both in the  $I$  and the  $1.6 \mu\text{m}$  bands, permitting some constraints on its form. If the excess is from dust which is heated by the cluster stars to 2000 K, its distance from the stars is  $\lesssim 100$  stellar radii; that is, the dust must be circumstellar.

Tables 5 and 6 give the best-fitting model parameters for the sources in the two galaxies, with the full tables again provided in the journal's electronic edition. Figure 20 shows the ages and extinctions for the sources in the two galaxies, regardless of the

acceptability of the fits. Given the IR-excess phenomenon described above, the best fits can still provide good estimates of the ages and the extinctions. Since the parameters of sources detected in only a few bands are poorly constrained, we fit only those sources detected in four or five bands (258 sources in NGC 1512 and 328 in NGC 5248). Point sizes are proportional to  $V$  brightness, and points have been given small arbitrary vertical and horizontal shifts to avoid overlap. The vertical striping pattern in the plots is the result of the discrete grid of models used. There is generally good agreement between the individual ages and extinctions deduced from the color-color diagrams in Figure 15 (for those clusters that have a UV measurement) and those found from model-fitting, as listed in Tables 5 and 6. The model-fitting, however, includes data from two additional bands, and is therefore sometimes more constrained.

In NGC 1512, most of the sources are best fit by model clusters that are 20 Myr or younger, and have low extinctions,  $0 < A_V < 1$  mag. In NGC 5248, the youngest and brightest sources are somewhat redder, with  $A_V \approx 1$  mag, as already concluded on the basis of color-color diagrams. The remaining sources cover a larger range in age than in NGC 1512, but here too, almost all have extinctions  $0 < A_V < 1$  mag, and ages 40 Myr or younger. There is, however, a significant fraction of clusters in both galaxies that are best fit with older models, of ages  $\sim 100$  Myr.

At first sight, this result is contrary to that expected, if the starbursts in the rings were continuous. The clusters fade by a factor less than 10 over 300 Myr (see Fig. 13), and the massive ones thus remain well within our dynamic range for this entire age range. In a continuous burst scenario, one would therefore naively expect many more clusters to have large ages, and one would conclude from the figures that the starbursts in each of these galaxies are episodic events which last only several tens of Myrs. However, we show here that the scarcity of old clusters may be the result of an age bias which causes young clusters to be over-represented at every luminosity.

Many studies of SSCs in various environments have shown that the clusters follow a steep luminosity distribution,  $N(L)dL \propto L^\alpha dL$ , with  $\alpha \approx -2$  (e.g., Meurer et al. 1995; Barth et al. 1995; Maoz et al. 1996; Whitmore et al. 1999; Carlson et al. 1999). Figure 21 shows the extinction-corrected  $V$ -band luminosity functions for the clusters in NGC 1512 and NGC 5248, separated into young ( $\leq 15$  Myr) and old ( $> 15$  Myr) categories. Each cluster’s age and extinction are based on its best-fit model. We have also plotted on the diagrams suitably normalized  $N(L)dL \propto L^{-2}dL$  power laws. The figures show that the cluster  $V$  luminosities in the two galaxies, when considering only the brightest clusters that are less susceptible to incompleteness, are consistent with an  $L^{-2}$  distribution, as has already been demonstrated for their 2300 Å luminosities by Maoz et al. (1996). More

importantly, the figures show that the individual “young” and “old” categories appear to follow the same distributions, although the small number of old clusters makes this statement tentative. Recalling the relatively small, but significant, fading of clusters with age, the evolution of the young stellar population can be simply described by a horizontal shift to the left of the luminosity functions shown in logarithmic coordinates in Figure 21. Because of their steep slopes, such effective age correction would make the old clusters intrinsically more abundant than the young ones, even for a luminosity shift by a factor of only a few. Thus, the fact that one sees relatively so many young clusters in these galaxies is not necessarily because the entire starburst is young. Instead, it could be the result of the fact that there are many more low-mass clusters than high-mass clusters. When the low-mass clusters are young, the moderate rise to a higher luminosity makes them more abundant than the older, higher-mass clusters that have the same luminosity.

The relative numbers of young and old clusters are thus consistent with continuous star formation. If, on the other hand, the star formation were episodic, we would expect few or no old clusters to be detected at all. Turning around the question of a continuous versus an episodic starburst, we can then ask whether an episodic starburst can be ruled out. One must recall that the best-fit models are not the *only* models that can fit each observed SED. Even with the considerable leverage afforded by the large wavelength range of our data, there is still degeneracy in assigning ages and extinctions to some clusters. Figure 22 shows, for every well-observed SED, the youngest model that is marginally consistent ( $\chi^2 \leq 2$  per degree of freedom). These models are also listed in Tables 5 and 6. The plots show that, if pushed, the data allow all but a handful of sources to be modeled as young clusters. It is thus possible that there are actually few old clusters in the galaxies. This could come about if the starbursts in the rings occur in  $\sim 20$  Myr-long episodes, with quiescent intervals of  $\sim 100$  Myr, or more. The same phenomenon could also occur if most of the clusters do not survive for longer than  $\sim 20$  Myr.

For completeness, Tables 5 and 6 also list, for each well-observed SED, the *oldest* model that is marginally acceptable. One sees that, in this case, there are many clusters that cannot be older than a few Myr, as already concluded based on the color-color diagrams.

### 3.3.6. Model Fitting – Cluster Masses

A total cluster mass can be associated with a model SED with a particular luminosity normalization. The total mass is that which is reached asymptotically by the decaying burst of star formation, but without accounting for mass loss from the cluster due to stellar winds and supernovae, which is theoretically difficult to predict. The total mass in

an observed cluster is necessarily uncertain when derived based on photometric (rather than kinematic) data. Most of the mass is in low-mass stars on the main sequence, which contribute negligibly to the light at any band. The total mass would increase by a factor of 2.55 or decrease by a factor of  $\sim 3$  if the low-mass cutoff were at  $0.1M_{\odot}$  or  $5M_{\odot}$ , respectively, instead of at  $1M_{\odot}$ . For young ( $\sim 1$  Myr) clusters, the total mass would increase by about 50% if the upper-mass cutoff were at  $30M_{\odot}$ , rather than at  $120M_{\odot}$ , because in the latter case, the very massive stars briefly dominate the luminosity, and fewer intermediate-mass stars are needed to explain the observed flux. Thus, compounding the theoretical uncertainties with the observational errors (e.g., the luminosity, and hence the mass, scales with the distance squared, and the distances to these galaxies are poorly known), the total masses we will derive below are uncertain to at least an order of magnitude, although this uncertainty may involve a systematic shift for all clusters, if all are similar in their star-formation parameters.

Recently, Zhang & Fall (1999) have used age and extinction estimates to show that, in the merging galaxies NGC 4038/9, the mass function of the clusters follows a power law similar to the luminosity function,  $N(m)dm \propto m^{-2}dm$ , over the range  $10^4 \leq m \leq 10^6 M_{\odot}$ . The mass function is important for understanding the relation between SSCs and old globular clusters. Our model fits to the clusters in NGC 1512 and NGC 5248 assign masses to each cluster, and allow extending this type of analysis to two more galaxies and a different starburst environment. Tables 5 and 6 list the masses for each of the fitted models. Figures 23 shows the mass functions for the clusters, based on the best-fit models. Although we are limited by incompleteness at low masses (low-mass clusters are faint) and small numbers at high masses (high-mass clusters are rare), the data are consistent with the same power-law mass distribution seen in NGC 4038/9.

The few, most massive, clusters in NGC 1512 and NGC 5248 have masses of  $\sim 10^5 M_{\odot}$ . Zhang & Fall (1999) found several tens of clusters in NGC 4038/9 with masses between  $2.5 \times 10^5 M_{\odot}$  and  $10^6 M_{\odot}$ . However, in making this comparison, two points need attention. First, the models of Zhang & Fall are generally similar to ours, but assume an IMF with a low-mass cutoff of  $0.1M_{\odot}$ , and hence their mass estimates are systematically higher by a factor of 2 than ours. Second, NGC 4038/9 is a more extended starburst than those in the nuclear rings, and therefore includes more clusters – Zhang & Fall derive masses for about 1600 clusters, whereas we do so for only about 300 in each galaxy. Given the steeply falling mass function, there is a low probability of finding in the ring galaxies clusters with the same masses as the few most massive ones in the merging galaxies. After accounting for these differences, the fraction of the cluster population above a given mass is similar in all three starburst systems.



### 3.3.7. Cluster Sizes

While some early studies with *HST* of SSCs in starburst environments claimed that the clusters were resolved, with sizes of order 10 pc (e.g., Whitmore & Schweizer 1995), recent studies of galaxies at  $\sim 10$  Mpc distances have generally concluded that the clusters are unresolved, or marginally resolved with the PC on WFPC2, corresponding to sizes of just a few pc or less. Specifically for the two galaxies examined here, Maoz et al. (1996) examined the radial profiles of the clusters in aberrated FOC F220W images. They concluded that the flux profiles, if modeled as Gaussians convolved with the PSF, have a dispersion ( $\sigma$ ) near or below the resolution limit, corresponding to a Gaussian radius of  $\lesssim 2$  pc. We re-examine the size question in the present, post-refurbishment, images of the clusters in NGC 1512 and NGC 5248, now taken in optical and IR bands.

We have carried out two tests to gauge the degree to which the sources are resolved. First, we studied the azimuthally averaged radial profile of the brighter sources, as in Maoz et al. (1996), but starting from a radius of 1 pixel and outwards. We attempted to fit the radial profiles with those of artificial PSFs produced by Tiny Tim (see §2), or with those observed for some of the brighter isolated sources in the images themselves (to see if there is a range of source sizes in the data). We find that, as in the UV, the sources seem to be unresolved or marginally resolved in the optical and IR. The result is not surprising in the IR, since the angular resolution is considerably worse than in the optical.

Second, we compared the ratio of counts within 1-pixel and 3-pixel radii that we obtained for the clusters in the F547M band (which has the best angular resolution) to the ratio obtained for artificial PSFs. Various authors (e.g., Barth et al. 1995; Whitmore et al. 1999) have used this so-called  $\Delta m_{1-3}$  test, or similar indicators, as a way of measuring sizes, with  $\Delta m_{1-3}$  significantly larger than that of the PSF indicating resolved sources. Tables 3 and 4 list  $\Delta m_{1-3}$  for all sources. We find that the Tiny Tim PSF for F547M has  $\Delta m_{1-3}=0.79$  mag, in good agreement with the Barth et al. (1995) value of 0.83 mag. To study the effect of the PC pixelation on  $\Delta m_{1-3}$ , we created also a Tiny Tim PSF in which the position of the source was on the corner of a pixel. (This is not a standard Tiny Tim option, and required creating a subsampled PSF, shifting and rebinning it, and convolving it with a kernel that simulates charge diffusion.) For this PSF,  $\Delta m_{1-3} = 1.02$  mag.

To get a direct empirical evaluation of  $\Delta m_{1-3}$ , one would ideally measure it for obvious foreground stars appearing on the same exposures, but there are only one or two such stars in these high Galactic latitude exposures. Instead, we measured  $\Delta m_{1-3}$  for the 100 brightest stars in an F547M image of the globular cluster NGC 6441. The total counts for these stars are comparable to those of the brightest sources in the two galaxies, and we used only the less crowded half of the PC1 image of the globular cluster, where the crowding is

similar to that in the circumnuclear rings. Figure 24 compares the distribution of  $\Delta m_{1-3}$  for the globular cluster stars with the values for the 10 brightest clusters in each galaxy. Also shown, with filled symbols, are the two measurements based on ideal artificial PSFs. The filled triangle represents a red, isolated,  $V = 21$  mag object in NGC 1512 (PC1 coordinates 664, 625), possibly a foreground star. A similarly red object (not plotted in Fig. 24) is found in NGC 5248 (PC1 coordinates 425, 385), in a high surface-brightness region, and has  $\Delta m_{1-3} = 2.12$ . While the distribution of  $\Delta m_{1-3}$  for the stars indeed peaks near 0.8, there is a tail to higher values of  $\Delta m_{1-3}$ , which encompasses many of the SSCs. We have repeated this experiment with the F547M image of another globular cluster, NGC 5139, which has a less crowded stellar field. In this case, there appears to be less of a high- $\Delta m_{1-3}$  tail, but the number of stars is small. Examination of the cases with  $\Delta m_{1-3} > 1$  in the first globular cluster shows that these are stars projected close to other stars of comparable brightness, confirming that source crowding can have a major influence on  $\Delta m_{1-3}$ .

The comparison with the globular clusters is not straightforward. The globular clusters were observed about two years before the galaxies, when the telescope focus may have differed. Their exposures are only 80 s and 50 s, much shorter than those of the galaxies, and may hence suffer less from image-degrading effects such as jitter. The stellar crowding in the globular clusters differs in its details from the crowding among the sources in the galaxies, which are also superimposed on a complex diffuse background. Given these uncertainties, we conclude that the bright clusters in NGC 1512 and NGC 5248 which have  $\Delta m_{1-3} > 1.1$  are possibly resolved, barring some of the possible systematics we cannot address. For the remaining bright clusters, it is unclear whether the  $\Delta m_{1-3}$  values, which are only slightly larger than those of isolated PSFs, are due to crowding or to truly resolved sizes.

We suspect that various reports of resolved SSCs in other starburst galaxies (e.g., Carlson et al. 1999) based on comparison of  $\Delta m_{1-3}$  analogs to artificial PSFs, neglecting the various systematic effects, may have overestimated the SSC sizes. Some of these other galaxies are significantly more distant than those studied here (e.g.,  $\sim 50$  Mpc for NGC 3597 in the Carlson et al. 1999 study). At such large distances, there is a larger chance of size errors due to crowding and confusion, especially since the brighter clusters tend to be spatially correlated. In the nearest examples, such as NGC 1569, the SSCs appear extremely compact as well, suggesting a distance-related bias. Since our tests indicate that the sources are unresolved or marginally resolved, we will not attempt further to derive physical sizes. Instead we note that, assuming a generic distance of 10 Mpc, the Gaussian radii of all the discrete sources are  $\lesssim 2$  pc.

#### 4. Discussion and Conclusions

We have analyzed broad-band and narrow-band images of two circumnuclear ring galaxies, obtained with the fine angular resolution of *HST*, and spanning a large continuum wavelength range, from 0.23 to 1.6  $\mu\text{m}$ , and two main emission lines,  $\text{H}\alpha$  and  $\text{Pa}\alpha$ . The data provide a uniquely detailed look into the properties and interrelations of the gas, the dust, and the compact clusters. Our main findings are as follows.

There is only a loose spatial correlation between the observed young clusters and the ionized gas in the rings. In some H II regions, no continuum sources are seen, and the presence of an embedded young population is revealed only by means of the high  $\text{Pa}\alpha$  equivalent width. In others, the ionized gas is in shells or bubbles surrounding complexes of clusters, which are apparently in the process of destroying their birth clouds. The  $\text{H}\alpha/\text{Pa}\alpha$  ratios of the line-emitting gas generally indicate only moderate extinction by a foreground screen, or, more realistically, an optically thick mixture of gas and dust. The latter option would explain the severe extinction, even at IR wavelengths, of the light from the young stars embedded in many of the clouds. Ionizing photon budget estimates also suggest that a large fraction of the ionizing stellar population is hidden. Unfortunately, because the line emission is probably also strongly extinguished by dust, it is difficult to say what this fraction is.

Comparison to other imaging studies of nearby starbursts, whether in rings or other configurations (e.g., Whitmore et al. 1999; Buta et al. 2000; Lancon et al. 2001), reveals a recurring pattern, whereby the continuum and line emission come from distinct sites. Although the visibility of the continuum sources depends on their ages (it takes time for them to break out of their clouds), there seems to be a strong element of geometry, orientation, and variation from galaxy to galaxy in determining what fraction of the clusters in a starburst is visible. For example, all the data point toward a generally dustier environment in NGC 5248 than in NGC 1512. This suggests that, on an individual galaxy basis, it is difficult to construct a coherent picture of stellar populations, gas content, and dust properties, based on measurements integrated over large areas of a starburst (as is unavoidable when angular resolution is limited, or a galaxy is distant).

This situation has led in the past to challenges in explaining self-consistently various subsets of spatially integrated measurements, such as the UV spectral slope, the  $\text{H}\alpha/\text{H}\beta$  intensity ratio, and the IR luminosity, both in nearby starbursts (e.g., Calzetti, Kinney, & Storchi-Bergmann 1994, 1996; Meurer et al. 1995, 1997), and in distant ones (e.g., Pettini et al. 1998; Meurer, Heckman, & Calzetti 1999). The common explanations have been that starbursts have a relatively grey extinction curve, or that the young stars and the gas have different spatial distribution. Takagi, Arimoto, & Vasevicius (1999) and Gordon et

al. (2000) have addressed this problem by considering also IR and sub-mm measurements, compared with stellar synthesis models that include the effects of mixed dust in various geometries. Charlot & Fall (2000) have extended those studies by accounting for absorption by various interstellar components, and limiting the lifetimes of some of the components as a result of their destruction by the new stars. They find they can reproduce the mean properties of starburst galaxies if the extinction law is grey, or if the extinction is steep but the dust has a patchy distribution. The data we have presented clearly support the latter picture.

We have measured the properties of the compact clusters in the rings, and analyzed them by means of traditional color-color diagrams, but also using explicit model fitting that exploits all the available information over the five continuum bands we have sampled. This improves our ability to separate the effects of age and extinction. Given the observational errors and the remaining age-extinction degeneracy in some cases, most of the SEDs are well fit by a range of spectral synthesis models. However, some of the brightest clusters reveal an IR excess that is not reproduced by any model. In most objects, the excess shows up only in one band, at  $1.6\ \mu\text{m}$ , and hence it is difficult to constrain its properties. In one object, where the IR excess is particularly large, and there is some excess emission in the  $I$  band as well, we have shown that the excess can be fit with a roughly 2000 K thermal spectrum. Since the bulk of the stellar radiation is from stars with effective temperatures of  $\sim 20000\ \text{K}$ , if the excess is the result of thermal reradiation by dust, the dust particles will be at no more than about 100 stellar radii, i.e., they are circumstellar dust shells. This result needs to be confirmed with additional observations, especially at longer IR wavelengths, which would probe the shape of the excess spectrum.

We find that the brightest clusters in both galaxies have ages of a few Myr, and undergo only mild extinction. The typical extinctions are  $A_V = 0.5\ \text{mag}$  in NGC 1512 and  $A_V = 1\ \text{mag}$  in NGC 5248. The extinction of clusters thus appears to be an “on/off” phenomenon, with the clusters either completely hidden in their birth clouds (and revealed only via the strong line emission from the clouds), or almost completely exposed. This shows that the stellar and supernova winds which presumably clear out the gas are extremely efficient in clearing out the gas on timescales  $\lesssim 1\ \text{Myr}$ .

The SEDs are well fit when assuming a steep, Galactic extinction law, consistent with the conclusion, above, regarding the form of the extinction law. Our best-fit models to the observed cluster SEDs suggest the presence also of older clusters, aged up to 300 Myr. However, given the uncertainties, almost none of these clusters can be ruled out from instead being 20 Myr or younger.

The clusters have a  $V$ -band luminosity function of the form  $N(L)dL \propto L^{-2}dL$ , similar

to that previously measured in the UV for these galaxies and to what is generally found for clusters in starburst environments. We have pointed out an “age bias,” where the steep luminosity function and the fading of clusters with time combine to make young clusters appear overabundant. The small fraction of old clusters indicated by the best-fit models is consistent with expectations if the starbursts in the rings are actually continuous, rather than episodic.

Evidence that other ring starbursts are episodic, rather than continuous, has been presented before, using similar age dating arguments (e.g., Smith et al. 1999; Pérez-Ramírez et al. 2000). Buta et al. (2000) have emphasized the possible detection of *some* old ( $> 50$  Myr) clusters in the ring in NGC 1326. From the theoretical perspective, Elmegreen (1994) has shown how a long period of gas accretion onto the region of the ring can lead to a synchronized starburst when a critical gas density is reached, and which may last only briefly, until the accreted gas is depleted. We caution that the age bias needs to be taken into account when deducing the star-forming history of a galaxy from its cluster age distribution. In the case of the galaxies analyzed here, because we cannot rule out the near absence of old clusters, we cannot exclude, based on the cluster ages, either of the possibilities, continuous or episodic, or the possibility that clusters are destroyed before they have a chance to age.

A statistical argument against episodic star formation can, however, be made. The UV imaging survey of Maoz et al. (1996) included an unbiased selection of 110 nearby galaxies from a complete sample. In the observed sample, 71 galaxies were spirals of Hubble type Sc or earlier, and 52 were classified as barred (SB or SAB) by de Vaucouleurs et al. (1991). In this sample, Maoz et al. found five examples of UV-bright circumnuclear rings. Accounting for incompleteness due to the limited field of view raised this number to seven, or about 10% of the Sc, and earlier, spirals. If circumnuclear starbursts are episodic, the models with the lowest acceptable ages suggest that the UV-bright phase lasts 10-20 Myr, while the interval between successive bursts is  $\gtrsim 100$  Myr. This would mean that most, or all, early-type spiral galaxies undergo occasional circumnuclear starbursts. While this possibility is not completely outlandish, it is contrary to the idea that circumnuclear rings require special conditions that are found only in some galaxies, which have strong bars and Lindblad resonances that channel gas accretion onto the rings (e.g., Elmegreen 1994).

The extensive broad-band data presented here, combined with our modeling, allow us to derive approximate masses and mass functions for the clusters. The mass function in the two galaxies is consistent with the  $N(m)dm \propto m^{-2}dm$  form that has been found in the only other starburst system, the Antennae galaxies, where this has been reliably measured (Zhang & Fall 1999). This power-law distribution is distinct from the log-normal

distribution observed for old globular clusters, which has a characteristic mass scale. If SSCs are the progenitors of globular clusters, some evolutionary process, such as evaporation or tidal disruption by galactic gravitational fields, must reshape the mass functions (Elmegreen & Efremov 1997; Fall & Zhang 2001).

The most massive clusters in NGC 1512 and NGC 5248 have masses in the range  $10^4$  to  $10^5 M_\odot$ . After accounting for statistics and differences in model parameters, this is similar to the masses in the Antennae. Combined with the other SSC characteristics we have evaluated, there is a remarkable uniformity in the properties of young clusters in these two different starburst environments.

We have estimated the sizes of the brighter, isolated SSCs, and argued that in some cases they are only marginally resolved, or unresolved, corresponding to Gaussian radii smaller than a few pc. Some previous size measurements of SSCs in other galaxies have probably not taken full account of the systematics which can artificially broaden the image of a point source. It is also possible that SSCs in different environments have different sizes. It is easy to show (e.g., Maoz et al. 1996) that the virial radius,  $r$ , the mass,  $m$ , and the age,  $t$ , together determine whether or not a cluster is gravitationally bound, where, for a bound cluster,

$$\left(\frac{t}{10^5 \text{ yr}}\right)^{-1} \left(\frac{r}{\text{pc}}\right)^{3/2} \left(\frac{m}{10^4 M_\odot}\right)^{-1/2} < 1.$$

The parameters we have derived for most of the brighter clusters establish them as bound objects, unless our mass estimates are systematically high due to, e.g., an extremely top-heavy stellar IMF. Visual-band size measurements, such as above, are also an essential ingredient in the more robust kinematic estimates of SSC masses based on optical spectroscopy (Ho & Filippenko 1996a,b; Smith & Gallagher 2000; Sternberg 1998).

To summarize, our study of the starburst rings in NGC 1512 and NGC 5248 has led to the following main conclusions.

1. The young star clusters and the line-emitting gas have different spatial distributions. The gas is mixed with dust, making it optically thick, and effective at completely obscuring some of the young clusters, which are revealed only by the line emission from the gas.
2. Most of the clusters that are visible are only mildly reddened, suggesting that the processes that clear out the gas and dust are efficient and fast.
3. Some of the brightest young clusters have an IR excess that may be thermal reradiation by circumstellar dust.

4. The cluster SEDs are consistent with a range in ages, from 1 Myr to 300 Myr. Although only a minority appears to be old, an age bias that causes young clusters to be over-represented makes this fraction consistent with continuous star formation in the rings over the past  $\sim 300$  Myr. Due to the uncertainties in dating the clusters, we cannot rule out episodic,  $\sim 20$  Myr-long bursts of star formation, although the statistics of the occurrence of UV-bright nuclear rings in spiral galaxies argue against this possibility. A third possibility is that old clusters are, in fact, absent, but due to the destruction of clusters after  $\sim 20$  Myr.
5. The sizes of the clusters are of order a few pc, or less. Considering also the range of ages and the large masses we have established for the clusters, this confirms that they are gravitationally bound objects.
6. The luminosity functions and the mass functions follow a power-law distribution with index  $-2$ , as seen in other starburst environments. The lack of a mass scale means that subsequent evolution of the mass function is required, if some of the SSCs are to evolve into globular clusters.
7. There is remarkable similarity in the properties of the gas, dust, and clusters in different starbursts that have been studied in detail, whether in circumnuclear rings or in merging galaxies.
8. In NGC 5248, there is a previously unknown, inner, emission-line ring of radius 60 pc. In NGC 1512, we have found a peculiar compact emission-line source with  $\sim 7000 \text{ \AA}$   $\text{H}\alpha + [\text{N II}]$  equivalent width, which may be a young, Balmer-dominated supernova remnant.

We thank A. Pauldrach and R.-P. Kudritzki for providing us with their model atmospheres in advance of publication, and the anonymous referee for constructive comments. This work was funded in part by grants GO-6738 and GO-7879 from the Space Telescope Science Institute, which is operated by AURA, Inc., under NASA contract NAS 5-26555. D. M. and A. S. acknowledge support by a grant from the Israel Science Foundation. Research by A. J. B. is supported by a postdoctoral fellowship from the Harvard-Smithsonian Center for Astrophysics. A. S. acknowledges support by German-Israeli Foundation grant I-551-186.07/97. A. V. F. and L. C. H. acknowledge funding from NASA grant NAG5-3556.

## REFERENCES

- Alonso-Herrero, A., Rieke, G. H., Rieke, M. J., & Scoville, N. Z. 2000, *ApJ*, 532, 845
- Aretxaga, I., et al. 1999, *MNRAS*, 309, 343
- Arp, H., & Sandage, A. 1985, *AJ*, 90, 1163
- Barth, A. J., Ho, L. C., Filippenko, A. V., & Sargent, W. L. W. 1995, *AJ*, 110, 1009
- Beck, S. C., Turner, J. L., & Kovo, O. 2000, *AJ*, 120, 244
- Benedict, G. F., et al. 1993, *AJ*, 105, 1369
- Brandl, B., et al. 1996, *ApJ*, 466, 254
- Bruzual A., G., & Charlot, S. 1993, *ApJ*, 405, 538
- Buta, R., Crocker, D. A., & Byrd, G. G. 1999, *AJ*, 118, 2071
- Buta, R., Treuthardt, P. M., Byrd, G. G., & Crocker, D. A. 2000, *AJ*, 120, 1289
- Calzetti, D., Kinney, A. L., & Storchi-Bergmann, T. 1994, *ApJ*, 429, 582
- Calzetti, D., Kinney, A. L., & Storchi-Bergmann, T. 1996, *ApJ*, 458, 132
- Cardelli, J. A., Clayton, G. C., & Mathis, J. S. 1989, *ApJ*, 345, 245
- Carlson, M. N., et al. 1998, *AJ*, 115, 1778
- Carlson, M. N., et al. 1999, *AJ*, 117, 1700
- Conti, P. S., & Vacca, W. D. 1994, *ApJ*, 423, L97
- Drissen, L., Roy, J.-R., Robert, C., & Devost, D. 2000, *AJ*, 119, 688
- Elmegreen, B. G. 1994, *ApJ*, 425, L73
- Elmegreen, B. G., & Efremov, Y. N. 1997, *ApJ*, 480, 235
- Fall, S. M. & Zhang, Q. 2001, *ApJ*, submitted
- Gallagher, J. S., Homeier, N. L., & Conselice, C. J. 2000, in *Massive Stellar Clusters*, ed. A. Lançon & C. M. Boily (San Francisco: ASP), 258
- Gallagher, S. C., Hunsberger, S. D., Charlton, J. C., & Zaritsky, D. 2000, in *Massive Stellar Clusters*, ed. A. Lançon & C. M. Boily (San Francisco: ASP), 247
- Gordon, K. D., Clayton, G. C., Witt, A. N., & Misselt, K. A. 2000, *ApJ*, 533, 236
- Ho, L. C., & Filippenko, A. V. 1996a, *ApJ*, 466, L83
- Ho, L. C., & Filippenko, A. V. 1996b, *ApJ*, 472, 600
- Ho, L. C., Filippenko, A. V., & Sargent, W. L. W. 1995, *ApJS*, 98, 477



- Ho, L. C., Filippenko, A. V., & Sargent, W. L. W. 1997, *ApJ*, 487, 579
- Holtzman, J. A., et al. 1992, *AJ*, 103, 691
- Holtzman, J. A., Burrows, C. J., Casertano, S., Hester, J. J., Trauger, J. T., Watson, A. M. & Worthey, G. 1995, *PASP*, 107, 1065
- Holtzman, J. A., et al 1996, *AJ*, 112, 416
- Hummel, E., van der Hulst, J. M., & Keel, W. C. 1987, *A&A*, 172, 32
- Hunter, D. A., O’Connell, R. W., & Gallagher, J. S. 1994, *AJ*, 108, 84
- Hunter, D. A., O’Connell, R. W., Gallagher, J. S., & Smecker-Hane, T. A. 2000, *AJ*, 120, 2383
- Kennicutt, R. C., Jr. 1998, *ARA&A*, 36, 189
- Kennicutt, R. C., Jr., & Chu, Y.-H. 1988, *AJ*, 95, 720
- Kobulnicky, H. A., & Johnson, K. E. 1999, *ApJ*, 527, 154 (Erratum: 539, 1023)
- Krist, J., & Hook, R. 1997, *The Tiny Tim User’s Guide* (Baltimore: STScI)
- Kroupa, P., Aarseth, S., & Hurley, J. 2001, *MNRAS*, in press (astro-ph/0009470)
- Kurucz, R. L. 1992, *Revista Mexicana de Astronomia y Astrofisica*, vol. 23, 181
- Laine, S., Knapen, J. H., Pérez-Ramírez, D., Doyon, R., & Nadeau, D. 1998, *MNRAS*, 302, L33
- Lançon, A., Goldader, J.D., Leitherer, C., & Gonzalez-Delgado, R. M. 2001, *ApJ*, in press, astro-ph/0101327
- Larson, R. B., & Tinsley, B. M. 1978, *ApJ*, 219, 46
- Leibundgut, B., et al. 1991, *ApJ*, 372, 531
- Leitherer, C., & Heckman, T. M. 1995, *ApJS*, 96, 9
- Leitherer, C., et al. 1999, *ApJS*, 123, 3
- Maíz-Apellániz, J., Muñoz-Tuñón, C., Tenorio-Tagle, G., & Mas-Hesse, J. M. 1999, *A&A*, 343, 64
- Maoz, D., Barth, A. J., Sternberg, A., Filippenko, A. V., Ho, L. C., Macchetto, F. D., Rix, H.-W., & Schneider, D .P. 1996, *AJ*, 111, 2248
- Martin, P., & Belley, J. 1997, *A&A*, 321, 363
- Melnick, J., Moles, M., & Terlevich, R. 1985, *A&A*, 149, L24
- Meurer, G. R. 1995, *Nature*, 375, 742
- Meurer, G. R., Heckman, T. M., & Calzetti, D. 1999, *ApJ*, 521, 64

- Meurer, G. R., Heckman, T. M., Leitherer, C., Kinney, A., Robert, C., & Garnett, D. R. 1995, *AJ*, 110, 2665
- Meurer, G. R., Heckman, T. M., Lehnert, M. D., Leitherer, C., & Lowenthal, J. 1997, *AJ*, 114, 54
- Miller, B. W., Whitmore, B. C., Schweizer, F., & Fall, S. M. 1996, *AJ*, 112, 1839
- O’Connell, R. W., Gallagher, J. S., & Hunter, D. A. 1994, *ApJ*, 433, 65
- O’Connell, R. W., Gallagher, J. S., Hunter, D. A., & Colley, W. N. 1995, *ApJ*, 446, L1
- Pauldrach, A. W. A., Lennon, M., Hoffmann, T. L., Sellmaier, F., Kudritzki, R.-P. & Puls, J. 1998, in *Properties of Hot Luminous Stars*, ed. I Howarth, (San Fransisco: ASP), 258
- Pettini, M., Kellogg, M., Steidel, C. C., Dickinson, M., Adelberger, K. L., & Giavalisco, M. 1998, *ApJ*, 508, 539
- Pérez-Ramírez, D., Knapen, J. H., Peletier, R. F., Laine, S., Doyon, R., & Nadeau, D. 2000, *MNRAS*, 317, 234
- Quillen, A.C., & Yukita, M. 2001, *AJ*, in press (astro-ph/0008437)
- Ravindranath, S., & Prabhu, T. P. 1998, *AJ*, 115, 2320
- Roy, J., & Belley, J. 1993, *ApJ*, 406, 60
- Rupen, M. P., van Gorkom, J. H., Knapp, G. R., Gunn, J. E., & Schneider, D. P. 1987, *AJ*, 94, 61
- Salpeter, E. E. 1955, *ApJ*, 121, 161
- Schaller, G., Schaerer, D., Meynet, G., & Maeder, A. 1992, *A&AS*, 96, 269
- Shields, J. C., & Kennicutt, R. C., Jr. 1995, *ApJ*, 454, 807
- Smith, D., Herter, T., Haynes, M. P., & Neff, S. G. 1999, *ApJ*, 510, 669
- Smith, L. J., & Gallagher, J. S. 2000, in *Massive Stellar Clusters*, ed. A. Lançon & C. M. Boily (San Francisco: ASP), 90
- Smith, R. C., Kirshner, R. P., Blair, W. P., & Winkler, P. F. 1991, *ApJ*, 375, 652
- Sternberg, A. 1998, *ApJ*, 506, 721
- Stiavelli, M., Panagia, N., Carollo, C. M., Romaniello, M., Heyer, I., & Gonzaga, S. 1998, *ApJ*, 492, L135
- Strickland, D. K., & Stevens, I. R. 1999, *MNRAS*, 306, 43
- Tacconi-Garman, L., Sternberg, A., & Eckart, A. 1996, *AJ*, 112, 918

- Takagi, T., Arimoto, N., & Vansevicius, V. 1999, *ApJ*, 523, 107
- Thornley, M. D., Schreiber, N. M. F., Lutz, D., Genzel, R., Spoon, H. W. W., Kunze, D., & Sternberg, A. 2000, *ApJ*, 539, 641
- Turner, J. L., Beck, S. C., Gorjian, V., & Ho, P. T. P. 1999, *BAAS*, 195, 08.09
- Turner, J. L., Beck, S. C., & Ho, P. T. P. 2000, *ApJ*, 532, L109
- van den Bergh, S. 1995, *Nature*, 374, 215
- van den Bergh, S. 2000, *PASP*, 112, 932
- Whitmore, B. C., et al. 1993, *AJ*, 106, 1354
- Whitmore, B. C., & Schweizer, F. 1995, *AJ*, 109, 960
- Whitmore, B. C., Zhang, Q., Leitherer, C., Fall, S. M., Schweizer, F., & Miller, B. W. 1999, *AJ*, 118, 1551
- Zhang, Q., & Fall, S. M. 1999, *ApJ*, 527, L81

Table 1. Observation Log

Instrument & Scale	Filter	Description	Inv. Sensitivity	NGC 1512		NGC 5248	
				Exposure	UT Date	Exposure	UT Date
WFPC2 0''0455 pix <sup>-1</sup>	F336W	“ <i>U</i> ”	$5.613 \times 10^{-17}$	2500	05/03/99	2300	30/01/99
	F547M	“ <i>V</i> ”	$7.691 \times 10^{-18}$	900	05/03/99	900	30/01/99
	F814W	“ <i>I</i> ”	$2.508 \times 10^{-18}$	1100	05/03/99	1100	30/01/99
	F658N	H $\alpha$ + [N II]	$4.187 \times 10^{-15}$	5200	05/03/99	4800	30/01/99
NICMOS-2 0''0764 pix <sup>-1</sup>	F160W	“ <i>H</i> ”	$2.406 \times 10^{-19}$	2560	29/07/98	2304	24/08/98
	F187W	Pa $\alpha$ cont.	$3.184 \times 10^{-19}$	2560	29/07/98	2304	24/08/98
	F187N	Pa $\alpha$	$7.534 \times 10^{-16}$	2560	29/07/98	...	...
	F187N	Pa $\alpha$	$9.727 \times 10^{-16}$	...	...	2304	24/08/98

Note. — Inverse sensitivity is in units of erg s<sup>-1</sup> cm<sup>-2</sup> Å<sup>-1</sup> per count s<sup>-1</sup> for the broad and medium band filters, and in erg s<sup>-1</sup> cm<sup>-2</sup> per count s<sup>-1</sup> for the two narrow-band filters (F658N and F187N). Pa $\alpha$  falls on different parts of the bandpass in the two galaxies, resulting in different sensitivities. Exposure times in seconds. UT date format is DD/MM/YY.

Table 2. Emission-Line Complexes

No. (1)	X (2)	Y (3)	$\Delta\alpha['']$ (4)	$\Delta\delta['']$ (5)	Radius (6)	$f(\text{H}\alpha)$ (7)	$f(\text{Pa}\alpha)$ (8)	$f_\lambda(1.6\ \mu\text{m})$ (9)	$f(\text{H}\alpha)/f(\text{Pa}\alpha)$ (10)	$f(\text{Pa}\alpha)/f_\lambda(1.6\ \mu\text{m})$ (11)
<b>NGC 1512</b>										
1	446.	549.	5.53	−4.77	0''68	179.6	44.4	31.0	4.0	143
2	405.	534.	3.66	−5.44	0''68	255.2	50.5	59.2	5.1	85
3	352.	515.	1.25	−6.32	0''68	289.9	58.8	39.5	4.9	149
4	299.	450.	−2.49	−5.58	0''45	91.8	24.1	23.3	3.8	103
5	275.	434.	−3.80	−5.72	0''45	88.7	24.1	21.9	3.7	110
6	263.	352.	−6.60	−3.20	0''23	16.9	9.8	3.6	1.7	271
7	324.	243.	−7.64	2.39	0''23	18.5	4.5	1.7	4.1	268
8	361.	234.	−6.61	3.78	0''45	70.3	24.1	7.7	2.9	313
9	574.	394.	5.50	4.38	0''45	69.2	8.3	17.6	8.4	47
10	577.	428.	6.59	3.27	0''45	46.5	8.3	13.2	5.6	63
11	540.	536.	8.44	−1.58	0''45	51.0	12.1	9.4	4.2	128
<b>NGC 5248</b>										
1	310.	449.	3.25	4.61	0''32	30.6	10.7	9.6	2.9	111
2	333.	421.	2.97	2.99	0''18	16.9	8.8	5.9	1.9	149
3	277.	421.	5.19	4.24	0''18	1.2	4.9	1.3	0.2	361
4	269.	411.	5.73	4.03	0''18	1.9	6.8	1.3	0.3	515
5	272.	392.	6.04	3.21	0''18	17.0	6.8	1.9	2.5	349
6	342.	375.	3.65	0.96	0''27	35.2	8.8	18.6	4.0	47
7	329.	359.	4.52	0.62	0''32	35.8	9.7	23.9	3.7	41
8	342.	337.	4.50	−.54	0''23	27.1	3.9	14.3	7.0	27
9	228.	285.	10.18	−.05	0''18	7.8	6.8	0.7	1.1	943
10	310.	289.	6.84	−1.72	0''18	12.1	4.9	3.3	2.5	146
11	346.	285.	5.50	−2.69	0''27	17.5	11.7	13.1	1.5	89
12	386.	277.	4.10	−3.90	0''45	104.7	25.3	29.1	4.1	87
13	471.	266.	0.98	−6.24	0''32	21.8	13.6	8.0	1.6	170
14	509.	346.	−2.32	−3.93	0''91	358.0	72.0	118.9	5.0	61
15	543.	406.	−5.01	−2.31	0''36	33.8	20.4	16.8	1.7	121
16	580.	416.	−6.70	−2.75	0''36	8.8	21.4	3.8	0.4	566
17	531.	481.	−6.21	0.93	0''36	45.2	11.7	20.3	3.9	58
18	464.	489.	−3.74	2.74	0''23	21.8	6.8	11.7	3.2	58
19	444.	504.	−3.28	3.79	0''23	18.7	4.9	10.9	3.8	45
20	387.	564.	−2.37	7.44	0''18	13.6	3.9	2.1	3.5	186
21	528.	561.	−7.89	4.16	0''18	33.6	6.8	8.5	4.9	80

Note. — (2)(3) X and Y PC pixel coordinates; (4)(5) Offset in arcseconds from the galaxy nucleus (in NGC 1512: pixel coordinates 419.6, 390.7; in NGC 5248: pixel coordinates 422.16, 396.02), in the R.A. and Decl. directions; (6) Angular radius of circular aperture used for flux measurements; at a distance of 10 Mpc, 0.1'' corresponds to 5 pc; (7)(8) Line fluxes in units of  $10^{-16}\ \text{erg s}^{-1}\ \text{cm}^{-2}$ . At a distance of 10 Mpc this unit corresponds to a luminosity of  $1.2 \times 10^{36}\ \text{erg s}^{-1}$ .  $\text{H}\alpha$  denotes  $\text{H}\alpha + [\text{N II}]$  flux in the F658N filter, as explained in text; (9)  $f_\lambda(1.6\ \mu\text{m})$  in units of  $10^{-18}\ \text{erg s}^{-1}\ \text{cm}^{-2}\ \text{\AA}^{-1}$ ; (11)  $f(\text{Pa}\alpha)/f_\lambda(1.6\ \mu\text{m})$  in  $\text{\AA}$ .

Table 3. Compact Sources Brightest in  $V$  – NGC 1512

No.	X PC	Y PC	$\Delta\alpha$ [']	$\Delta\delta$ [']	$V$ mag	$\Delta_{1-3}$ mag	$f_\lambda$ 2300 Å	$\sigma$	$f_\lambda$ 3350 Å	$\sigma$	$f_\lambda$ 5490 Å	$\sigma$	$f_\lambda$ 8040 Å	$\sigma$	$f_\lambda$ 1.6 $\mu$ m	$\sigma$
(1)	(2)	(3)	(4)	(5)	(6)	(7)	(8)	(9)	(10)	(11)	(12)	(13)	(14)	(15)	(16)	(17)
1	407.42	534.64	3.76	-5.39	19.10	0.98	22000.0	4400.0	2957.5	149.8	755.9	38.9	237.0	12.4	39.9	4.0
2	350.21	512.03	1.10	-6.26	20.22	1.14	3450.0	690.0	1212.1	61.6	269.3	14.0	85.2	4.6	13.8	1.2
3	444.00	549.25	5.47	-4.84	20.31	1.05	1650.0	330.0	868.9	44.1	248.2	13.0	86.4	4.8	15.7	1.8
4	277.43	434.07	-3.71	-5.65	20.68	1.15	1360.0	272.0	555.7	30.6	176.4	9.7	70.8	4.1	14.4	2.5
5	398.78	528.47	3.28	-5.43	20.74	1.33	670.0	134.0	458.1	28.2	167.2	10.2	79.7	5.0	59.0	4.3
6	250.51	414.17	-5.23	-5.74	21.07	0.86	210.0	42.0	177.6	9.6	122.9	6.6	62.5	3.3	16.5	1.6
7	405.49	531.97	3.62	-5.35	21.19	3.09	< 30	...	488.4	29.8	110.3	8.6	50.9	4.1	22.6	2.9
8	444.72	545.52	5.38	-4.69	21.26	1.57	1000.0	200.0	432.6	23.1	103.4	6.4	35.6	3.0	14.4	1.6
9	548.57	317.11	2.37	6.33	21.38	1.06	270.0	54.0	194.2	10.8	92.0	5.4	39.4	2.1	8.9	0.8
10	573.71	392.75	5.45	4.41	21.51	1.52	610.0	122.0	266.2	14.2	82.3	4.8	30.3	2.2	8.6	0.9
11	541.50	526.25	8.21	-1.20	21.64	1.27	300.0	60.0	191.7	10.7	72.9	4.4	28.5	1.7	7.9	0.9
12	257.85	419.39	-4.82	-5.71	21.78	0.81	200.0	40.0	186.7	11.1	64.1	4.6	24.2	2.2	4.1	1.4
13	258.43	323.01	-7.61	-2.32	21.82	1.42	< 30	...	64.4	4.8	61.5	3.8	34.1	2.1	11.7	1.1
14	306.08	446.24	-2.36	-5.25	21.84	1.50	200.0	40.0	132.4	8.9	60.7	3.7	27.1	1.6	6.5	1.3
15	307.29	447.80	-2.27	-5.26	21.89	1.57	370.0	74.0	146.3	8.7	57.8	3.4	23.5	1.4	3.4	1.3
16	269.34	423.21	-4.31	-5.51	21.95	1.05	190.0	38.0	119.2	9.3	54.6	4.6	27.0	2.5	21.9	2.0
17	353.49	512.40	1.23	-6.18	21.98	3.14	< 30	...	214.9	13.0	53.2	4.2	25.3	2.3	9.6	1.0
18	272.16	427.69	-4.08	-5.58	22.09	1.50	240.0	48.0	151.2	10.8	48.0	4.2	15.1	2.1	14.7	2.0
19	300.79	446.65	-2.53	-5.41	22.12	1.04	320.0	64.0	185.1	10.8	46.6	3.8	14.0	1.3	2.5	1.2
20	256.38	321.62	-7.72	-2.33	22.14	1.60	< 30	...	72.5	5.1	45.9	3.1	27.8	1.6	9.2	1.0
21	296.04	454.57	-2.46	-5.83	22.14	1.05	270.0	54.0	135.5	8.3	45.7	3.5	16.4	2.4	< 1	...
22	439.91	196.02	-4.95	7.40	22.16	0.85	< 30	...	305.2	15.8	45.3	2.6	17.1	1.0	< 1	...
23	244.98	404.33	-5.71	-5.56	22.16	1.01	< 30	...	60.5	4.1	45.1	2.9	18.8	1.2	7.7	1.4
24	439.87	534.85	4.90	-4.45	22.18	1.29	< 30	...	60.0	6.7	44.2	3.6	34.6	2.5	30.7	1.8
25	280.84	451.00	-3.10	-6.15	22.20	1.12	90.0	18.0	94.2	6.8	43.5	3.5	15.0	1.8	4.8	1.5
26	593.89	475.05	8.55	2.12	22.20	1.46	140.0	28.0	74.1	5.3	43.5	3.0	23.9	1.6	11.9	1.2
27	443.00	534.75	5.01	-4.36	22.21	1.59	< 30	...	35.1	5.8	43.1	3.7	33.3	2.3	25.9	1.9
28	402.32	540.55	3.76	-5.75	22.25	1.64	< 30	...	125.0	7.9	41.5	3.3	18.0	1.8	13.7	1.2
29	603.75	721.68	16.07	-6.22	22.31	1.15	...	...	19.7	2.3	39.2	2.3	28.8	1.5	...	...
30	597.08	511.50	9.72	0.94	22.31	0.95	< 30	...	5.7	1.3	39.1	2.4	40.0	2.1	21.2	1.2

Note. — The complete version of this table is in the electronic edition of the Journal. The printed edition contains only a sample; (2)(3) X and Y pixel PC coordinates in the F547M frame; (4)(5) Offset in arcseconds from the galaxy nucleus (at pixel coordinates 419.6, 390.7) in the R.A. and Decl. directions; (6)  $V$  magnitude; (7) Magnitude difference between F547M photometry in 3-pixel- and 1-pixel-radius apertures; (8)-(17)  $f_\lambda$  and  $1\sigma$  errors in units of  $10^{-19}$  erg s $^{-1}$  cm $^{-2}$  Å $^{-1}$ . Missing entries are for sources outside the field of view of the FOC or NICMOS. For null detections, the flux limits actually depend on the local background and crowding, and the limits quoted are just those typical for the band.

Table 4. Compact Sources Brightest in  $V$  – NGC 5248

No.	X	Y	$\Delta\alpha$	$\Delta\delta$	$V$	$\Delta_{1-3}$	$f_\lambda$	$\sigma$	$f_\lambda$	$\sigma$	$f_\lambda$	$\sigma$	$f_\lambda$	$\sigma$	$f_\lambda$	$\sigma$
(1)	PC	PC	[ $''$ ]	[ $''$ ]	mag	mag	2300 Å	(9)	3350 Å	(11)	5490 Å	(13)	8040 Å	(15)	1.6 $\mu$ m	(17)
1	527.45	560.56	-7.86	4.16	18.26	0.91	2810.0	562.0	3510.9	176.4	1641.9	82.5	649.2	32.7	84.7	4.7
2	302.41	311.83	6.63	-0.65	19.64	0.84	300.0	60.0	621.6	31.8	460.1	23.8	209.9	11.0	28.5	3.8
3	330.29	312.58	5.51	-1.25	19.87	1.10	1110.0	222.0	806.3	42.3	370.5	19.8	168.2	9.4	108.4	7.7
4	280.13	324.35	7.23	0.34	20.15	0.97	530.0	106.0	522.4	27.0	287.8	14.8	129.9	6.7	44.9	3.4
5	411.89	262.85	3.39	-5.04	20.29	1.38	660.0	132.0	496.2	28.4	252.9	15.7	132.0	8.4	89.8	7.6
6	498.44	339.01	-1.74	-3.97	20.41	1.18	520.0	104.0	442.7	23.4	225.0	12.0	102.9	5.8	30.3	2.3
7	513.45	348.56	-2.55	-3.92	20.48	1.25	1220.0	244.0	733.9	38.8	211.1	12.1	72.0	4.2	17.1	2.3
8	554.06	478.15	-7.06	0.30	20.66	1.01	770.0	154.0	511.7	26.9	179.2	9.9	61.1	3.6	8.4	1.8
9	454.36	520.05	-4.05	4.19	20.71	1.02	430.0	86.0	447.5	23.4	171.5	9.5	63.2	3.9	15.3	2.6
10	502.67	343.70	-2.02	-3.88	20.77	1.01	230.0	46.0	337.3	19.2	162.2	9.6	69.4	4.9	9.8	1.6
11	346.77	268.92	5.83	-3.34	20.82	1.16	260.0	52.0	294.2	15.6	154.8	8.8	73.8	4.5	34.3	3.8
12	338.38	187.17	8.00	-6.39	20.88	1.01	410.0	82.0	327.8	17.3	146.2	7.8	58.3	3.2	18.4	1.4
13	344.61	375.92	3.52	0.94	20.93	1.23	350.0	70.0	333.2	17.7	140.3	8.5	52.1	4.0	5.7	1.7
14	515.11	349.60	-2.64	-3.92	20.96	1.92	< 30	...	422.3	24.2	136.3	9.1	55.1	4.8	18.5	2.7
15	504.04	342.91	-2.05	-3.94	21.10	2.26	230.0	46.0	242.4	14.8	119.2	7.8	53.6	3.9	12.9	1.7
16	496.68	336.63	-1.62	-4.02	21.17	1.96	< 30	...	218.2	12.2	112.3	6.4	62.1	3.8	16.2	2.1
17	535.25	481.75	-6.40	0.86	21.18	1.60	240.0	48.0	233.5	13.5	110.7	7.2	41.2	3.6	13.3	1.9
18	341.92	538.23	-0.01	7.43	21.26	1.13	240.0	48.0	191.3	10.6	103.0	6.0	56.4	3.3	35.5	2.5
19	531.00	570.30	-8.22	4.46	21.28	1.00	320.0	64.0	231.4	15.1	101.7	8.0	42.6	3.9	...	...
20	332.91	538.85	0.33	7.66	21.29	1.24	190.0	38.0	161.3	9.2	100.6	5.5	59.2	3.3	27.0	2.2
21	525.62	347.69	-3.01	-4.23	21.35	1.06	140.0	28.0	191.8	12.8	94.8	7.8	39.3	4.0	26.5	3.7
22	341.11	318.68	4.94	-1.25	21.39	1.50	< 30	...	150.5	10.9	91.4	7.6	46.9	4.9	23.2	4.9
23	280.47	340.22	6.86	0.97	21.42	1.28	220.0	44.0	158.7	8.9	89.1	5.2	49.3	3.0	16.5	3.1
24	342.77	364.74	3.84	0.54	21.45	1.42	< 30	...	136.4	14.4	86.5	12.0	35.1	6.0	29.8	2.7
25	341.16	374.71	3.68	0.97	21.48	1.55	160.0	32.0	227.8	13.2	84.3	6.3	36.5	3.4	9.5	2.0
26	342.99	374.29	3.62	0.91	21.50	2.42	350.0	70.0	206.2	12.4	82.9	6.7	40.0	3.9	11.8	1.8
27	443.86	379.88	-0.50	-1.13	21.55	2.03	< 30	...	67.9	5.8	79.0	8.1	52.4	6.9	< 1	...
28	431.58	376.18	0.07	-1.00	21.56	1.72	< 30	...	63.1	4.9	78.2	6.6	58.2	6.4	< 1	...
29	495.80	498.68	-5.22	2.42	21.59	1.34	230.0	46.0	177.0	10.1	76.5	5.2	31.8	2.7	9.9	1.7
30	407.68	264.10	3.53	-4.90	21.59	1.49	< 30	...	90.7	13.9	76.4	9.3	55.7	4.8	60.5	5.9

Note. — The complete version of this table is in the electronic edition of the Journal. The printed edition contains only a sample; (4)(5) Offset in arcseconds from the galaxy nucleus (at pixel coordinates 422.16, 396.02) in the R.A. and Decl. directions; other notes as in Table 3.

Table 5. Cluster Ages, Extinctions, and Masses – NGC 1512

No.	Bands	Age Myr	Best Fitting Model			Youngest Acceptable Model				Oldest Acceptable Model			
			$A_V$ mag	Mass $10^4 M_\odot$	$\chi^2/\text{dof}$	Age Myr	$A_V$ mag	Mass $10^4 M_\odot$	$\chi^2/\text{dof}$	Age Myr	$A_V$ mag	Mass $10^4 M_\odot$	$\chi^2/\text{dof}$
1	5	1	0.0	9.08	99.59	...	...	...	...	...	...	...	...
2	5	3	0.2	0.72	8.55	...	...	...	...	...	...	...	...
3	5	1	0.6	3.72	4.45	...	...	...	...	...	...	...	...
4	5	5	0.1	0.31	2.52	...	...	...	...	...	...	...	...
5	5	10	0.0	0.51	15.42	...	...	...	...	...	...	...	...
6	5	20	0.6	1.35	1.61	20	0.6	1.35	1.61	20	0.6	1.35	1.61
7	4	3	0.6	0.49	17.59	...	...	...	...	...	...	...	...
8	5	1	0.4	1.35	13.17	...	...	...	...	...	...	...	...
9	5	5	0.6	0.24	2.14	...	...	...	...	...	...	...	...
10	5	5	0.1	0.14	7.27	...	...	...	...	...	...	...	...
11	5	20	0.1	0.55	3.22	...	...	...	...	...	...	...	...
12	5	1	1.0	1.36	0.35	1	0.9	1.12	1.26	3	0.9	0.29	0.45
13	4	20	1.0	0.94	1.29	7	0.5	0.13	1.80	100	0.0	1.18	1.36
14	5	20	0.2	0.48	1.25	5	0.5	0.14	1.63	20	0.2	0.48	1.25
15	5	5	0.2	0.11	0.53	5	0.2	0.11	0.53	5	0.2	0.11	0.53
16	5	12	0.1	0.22	6.09	...	...	...	...	...	...	...	...
17	4	3	0.8	0.28	20.73	...	...	...	...	...	...	...	...
18	5	20	0.0	0.35	9.92	...	...	...	...	...	...	...	...
19	5	3	0.5	0.15	0.75	1	0.5	0.60	0.80	3	0.4	0.12	1.24
20	4	7	0.3	0.10	0.46	7	0.2	0.09	1.09	70	0.0	0.68	1.34
21	4	1	0.6	0.61	1.29	1	0.6	0.61	1.29	5	0.2	0.08	1.61
23	4	20	0.6	0.47	0.97	20	0.5	0.42	1.72	40	0.0	0.43	1.95
24	4	12	0.6	0.33	1.21	12	0.6	0.33	1.21	12	0.6	0.33	1.21
25	5	1	1.2	1.00	1.17	1	1.1	0.84	1.77	3	1.1	0.21	1.41
26	5	15	0.1	0.20	1.83	15	0.1	0.20	1.83	15	0.1	0.20	1.83
27	4	10	0.9	0.28	1.73	10	0.9	0.28	1.73	10	0.9	0.28	1.73
28	4	20	0.0	0.35	21.46	...	...	...	...	...	...	...	...
30	4	300	2.2	11.03	2.04	...	...	...	...	...	...	...	...

Note. — The complete version of this table is in the electronic edition of the Journal. The printed edition contains only a sample; Objects with detections in fewer than 4 bands not fitted. Formally “acceptable” models have  $\chi^2$  per degree of freedom  $< 2$ .



Table 6. Cluster Ages, Extinctions, and Masses – NGC 5248

No.	Bands	Age Myr	Best Fitting Model			Youngest Acceptable Model				Oldest Acceptable Model			
			$A_V$ mag	Mass $10^4 M_\odot$	$\chi^2/\text{dof}$	Age Myr	$A_V$ mag	Mass $10^4 M_\odot$	$\chi^2/\text{dof}$	Age Myr	$A_V$ mag	Mass $10^4 M_\odot$	$\chi^2/\text{dof}$
1	5	1	1.3	41.85	0.27	1	1.3	41.85	0.27	3	1.2	8.88	1.53
2	5	1	1.9	19.58	2.52	...	...	...	...	...	...	...	...
3	5	40	0.1	4.89	13.01	...	...	...	...	...	...	...	...
4	5	20	0.5	2.93	1.58	20	0.5	2.93	1.58	20	0.5	2.93	1.58
5	5	40	0.2	3.72	8.59	...	...	...	...	...	...	...	...
6	5	20	0.4	2.14	1.41	20	0.4	2.14	1.41	20	0.4	2.14	1.41
7	5	3	0.6	0.75	4.54	...	...	...	...	...	...	...	...
8	5	1	0.8	2.96	0.44	1	0.8	2.96	0.44	3	0.7	0.62	1.48
9	5	1	1.1	3.83	2.05	...	...	...	...	...	...	...	...
10	5	3	1.4	1.15	0.03	1	1.4	4.59	0.19	3	1.3	0.98	0.98
11	5	20	0.6	1.87	3.59	...	...	...	...	...	...	...	...
12	5	20	0.3	1.30	3.44	...	...	...	...	...	...	...	...
13	5	1	1.1	2.99	0.23	1	1.0	2.49	1.84	3	1.0	0.63	0.81
14	4	5	0.1	0.25	7.16	...	...	...	...	...	...	...	...
15	5	5	0.8	0.37	1.92	5	0.8	0.37	1.92	5	0.8	0.37	1.92
16	4	7	0.0	0.18	0.72	7	0.0	0.18	0.72	30	0.0	1.03	1.94
17	5	20	0.4	1.03	4.11	...	...	...	...	...	...	...	...
18	5	40	0.3	1.70	8.86	...	...	...	...	...	...	...	...
19	4	5	0.5	0.23	1.11	5	0.5	0.23	1.11	20	0.2	0.79	1.99
20	5	30	0.4	1.32	1.76	30	0.4	1.32	1.76	40	0.4	1.72	1.90
21	5	20	0.6	1.13	5.91	...	...	...	...	...	...	...	...
22	4	40	0.1	1.13	0.64	7	0.0	0.14	1.76	70	0.0	1.37	1.58
23	5	30	0.2	0.93	1.31	20	0.5	1.03	1.70	40	0.2	1.22	1.50
24	4	12	0.0	0.30	2.83	...	...	...	...	...	...	...	...
25	5	3	1.2	0.53	2.02	...	...	...	...	...	...	...	...
26	5	20	0.1	0.64	1.85	20	0.1	0.64	1.85	20	0.1	0.64	1.85
29	5	20	0.3	0.71	2.55	...	...	...	...	...	...	...	...
30	4	12	0.7	0.60	2.53	...	...	...	...	...	...	...	...

Note. — The complete version of this table is in the electronic edition of the Journal. The printed edition contains only a sample; See Table 5.

Fig. 1.— Multiwavelength view of NGC 1512. Each panel shows a section of the image that is  $18.2''$  on a side. Arrowed lines in the F547M panel show the orientation. The same scale and orientation apply to the subsequent images of this galaxy, in Figs. 3-9.

Fig. 2.— Same as Fig.1, for NGC 5248.

Fig. 3.— “True color” renditions of NGC 1512 and NGC 5248, with blue, green, and red representing F336W, F547M, and F814W, respectively.

Fig. 4.— Additional color composites of NGC 1512 (left) and NGC 5248 (right). From top to bottom: a UV-through-IR composite, with blue, green, and red representing F220W, F547M, and F160W, respectively; an emission-line image, similar to the true-color versions in Fig. 3, but with red representing the F658N image ( $H\alpha + [N\ II] + \text{continuum}$ ); an IR rendition, with blue, green, and red representing F814W, F160W, and F187W, respectively.

Fig. 5.— Continuum-subtracted images of NGC 1512 in  $H\alpha+[N\ II]$  (left) and  $Pa\alpha$  (right). The main emission-line complexes are labeled, and marked with the apertures used for the measurements in Table 2. The peculiar compact  $H\alpha+[N\ II]$  source discussed in the text is marked “A”.

Fig. 6.— Continuum-subtracted images of NGC 5248 in  $H\alpha+[N\ II]$  (left) and  $Pa\alpha$  (right). The main emission-line complexes are labeled, and marked with the apertures used for the measurements in Table 2.

Fig. 7.— Left:  $H\alpha + [\text{N II}]$  emission (contours) overlaid on the F336W image of NGC 1512 (greyscale). Right: Detail focusing on the upper left quadrant. Note the imperfect correspondence between the brightest  $H\alpha + [\text{N II}]$  and continuum knots. Lowest-level contours are at a level of  $8.7 \times 10^{-17} \text{ erg s}^{-1} \text{ cm}^{-2} \text{ arcsec}^{-2}$ , and the interior contours are at  $2.2 \times 10^{-16} \text{ erg s}^{-1} \text{ cm}^{-2} \text{ arcsec}^{-2}$  and  $5.4 \times 10^{-16} \text{ erg s}^{-1} \text{ cm}^{-2} \text{ arcsec}^{-2}$ .



Fig. 8.— Left:  $H\alpha + [\text{N II}]$  emission (contours) overlaid on the F336W image of NGC 5248 (greyscale). Right: Detail. Contour levels are as in Fig. 7.

Fig. 9.— Left:  $(\text{H}\alpha + [\text{N II}])/\text{Pa}\alpha$  emission line ratio map for NGC 1512. Right: Detail focusing on the upper left quadrant. Overlaid contours are the  $\text{Pa}\alpha$  emission, delineating the regions where there is significant detected flux in this line above a level of  $6 \times 10^{-16} \text{ erg s}^{-1} \text{ cm}^{-2} \text{ arcsec}^{-2}$ . The second contour corresponds to  $14 \times 10^{-16} \text{ erg s}^{-1} \text{ cm}^{-2} \text{ arcsec}^{-2}$ . The  $\text{Pa}\alpha$  image is shallower than the  $\text{H}\alpha + [\text{N II}]$  image, and limits the regions where the ratio can be measured reliably. Outside the outer marked contours, the ratio is dominated by noise and background residuals. The whitest regions correspond to a ratio of 1 or less, while the darkest areas have a ratio of 10 or more. Most pixels within the contours of significant  $\text{Pa}\alpha$  emission have a greyish shade, corresponding to ratios of about 4.

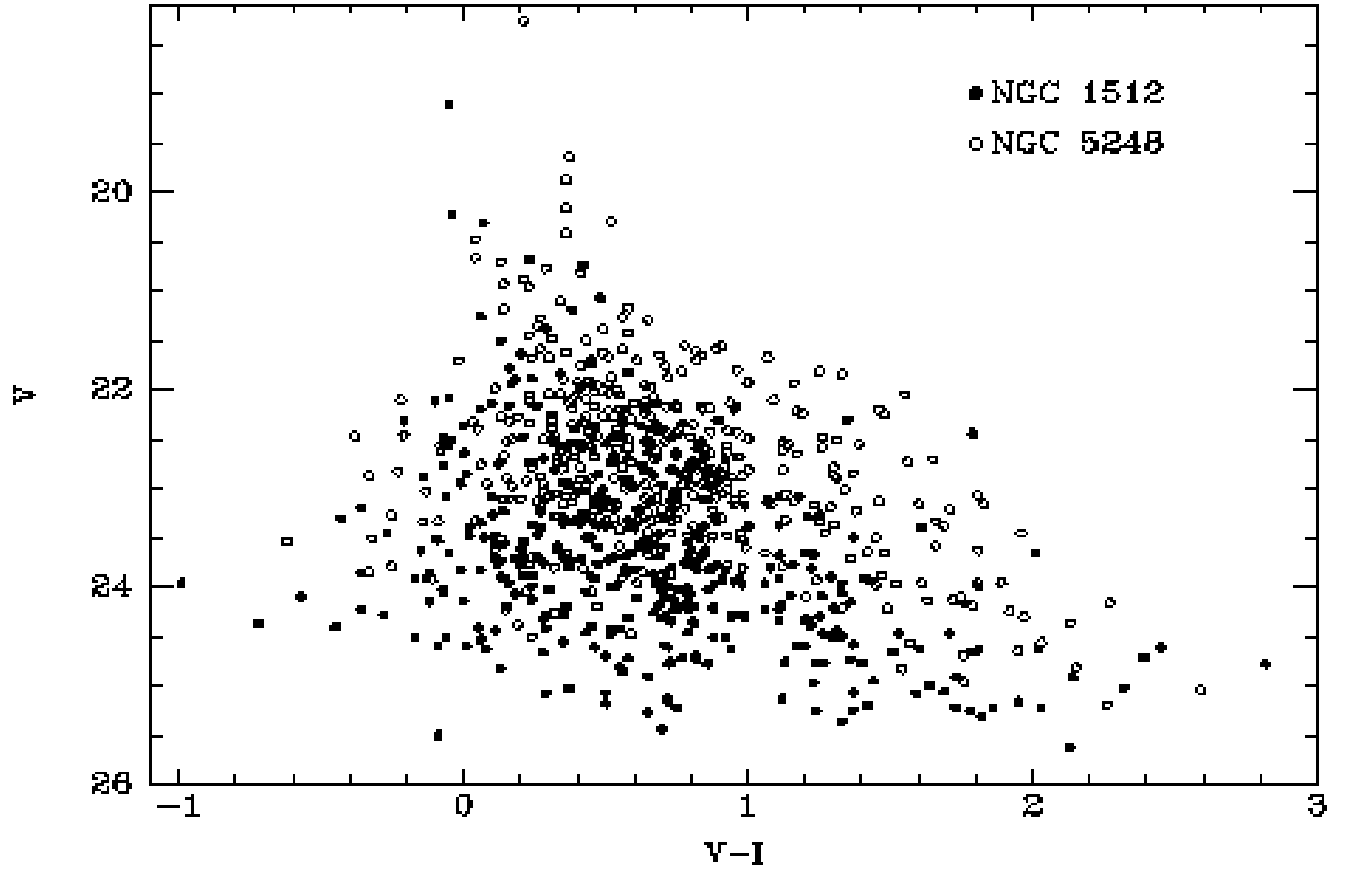


Fig. 10.— Color-magnitude diagram showing all of the sources detected in  $V$  and  $I$ . The sources in NGC 5248 have a larger spread in color than those in NGC 1512, and are typically 0.5-1 mag redder.

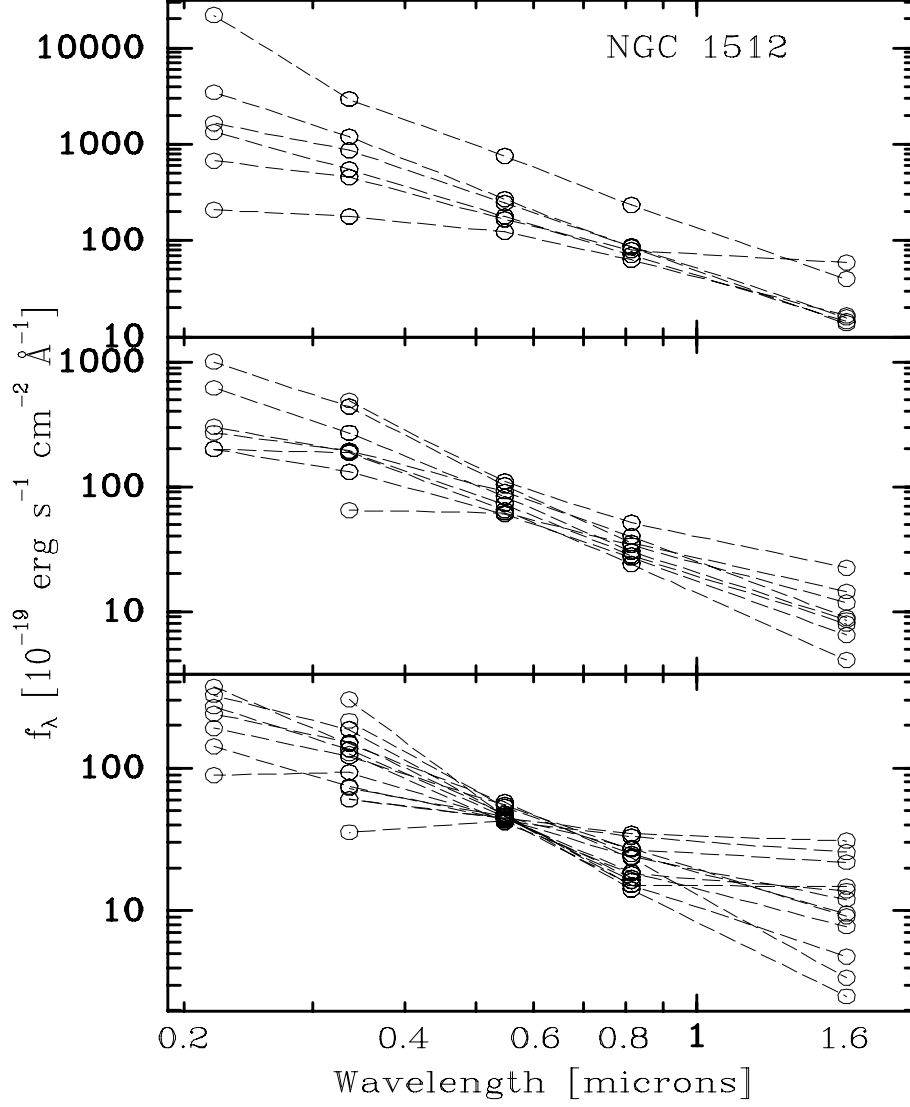


Fig. 11.— Spectral energy distributions (SEDs), from 0.22 to 1.6  $\mu\text{m}$ , of the 19 clusters that are brightest in  $V$  in NGC 1512, separated into three panels in decreasing brightness groups. Most of the brightest clusters are blue, indicating an age of a few million years, and little reddening. Error bars are omitted for clarity.

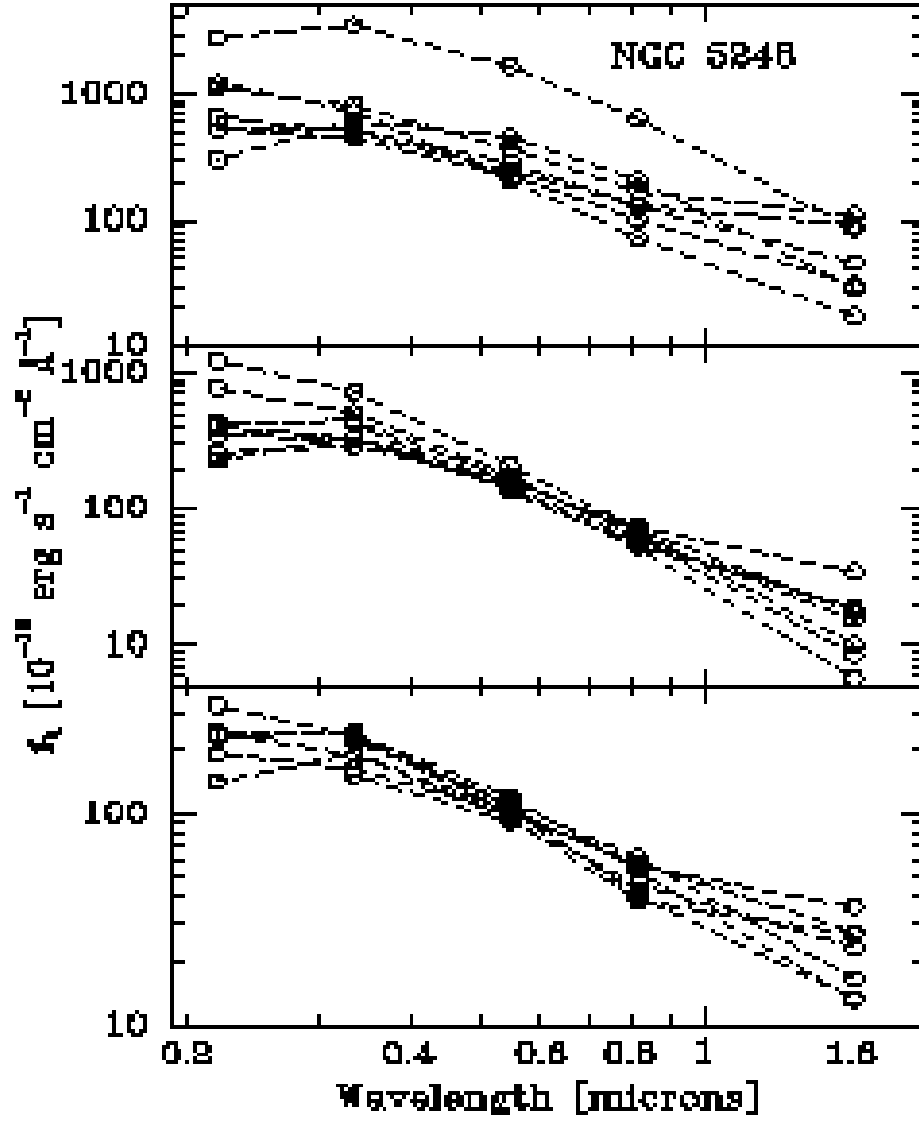


Fig. 12.— Same as Figure 10, but for the 21 clusters brightest in  $V$  in NGC 5248.

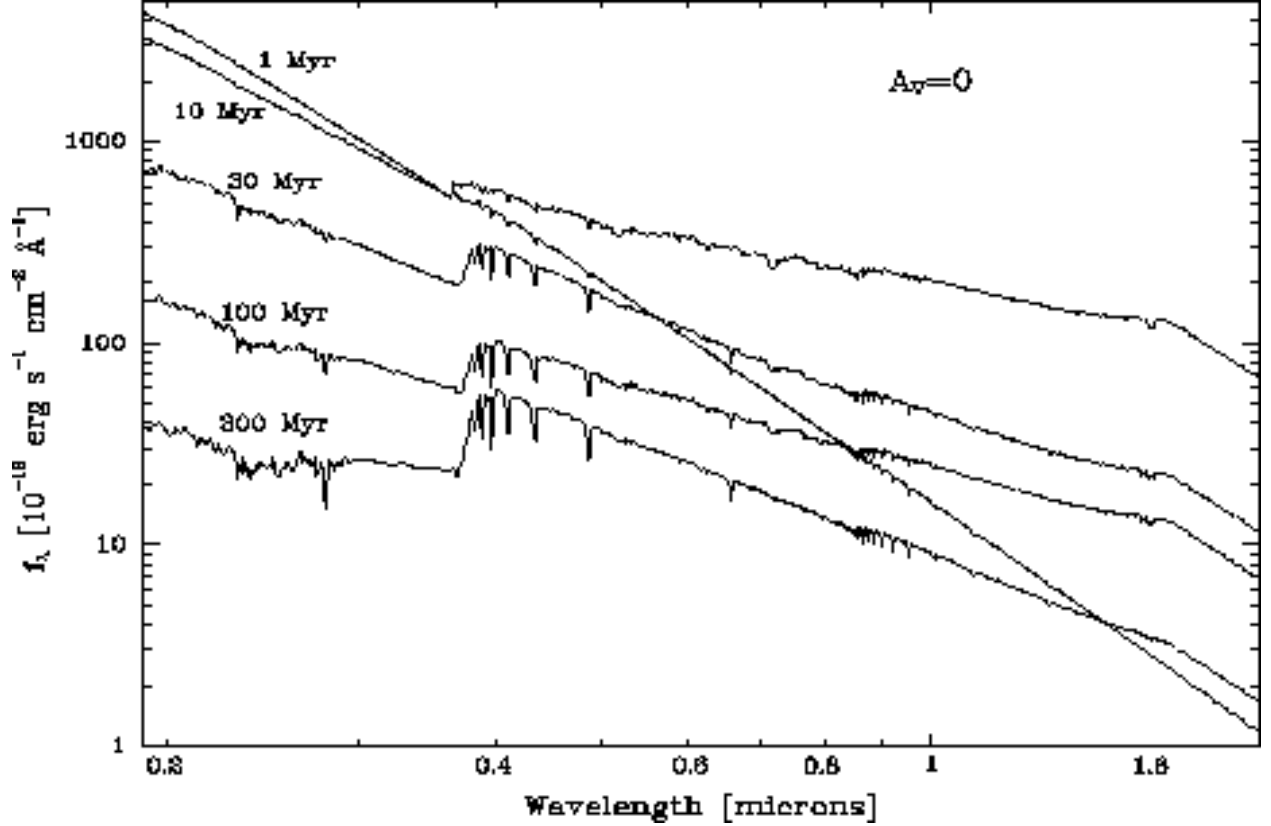


Fig. 13.— Examples of spectral synthesis models for an unreddened starburst population. All models assume a Salpeter IMF with upper and lower mass limits  $M_{up} = 120M_{\odot}$  and  $M_{low} = 1M_{\odot}$ , respectively, and an exponentially decaying star formation rate with a characteristic timescale of 1 Myr. An arbitrary vertical shift has been applied to the models as a whole (but not relative to each other), corresponding to a scaling with distance-squared or mass.

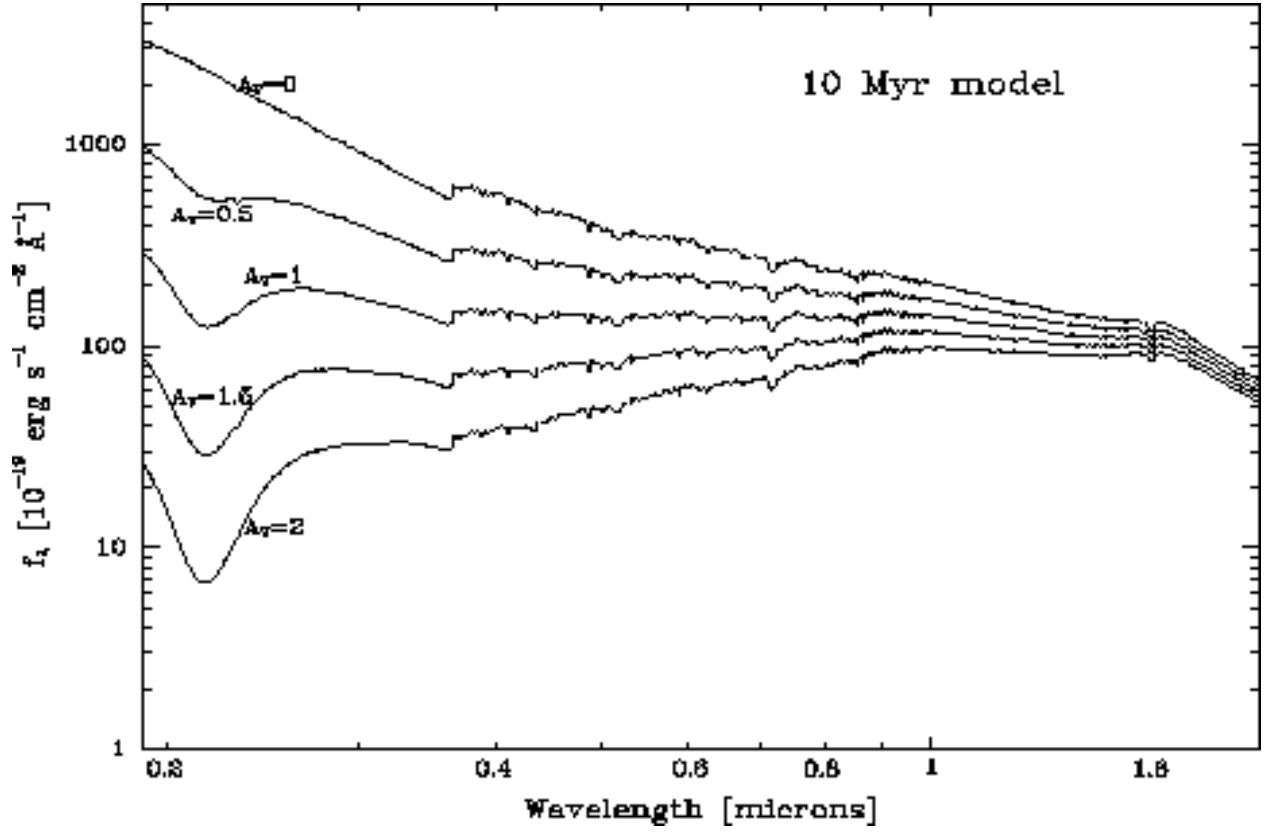


Fig. 14.— Illustration of the effects of foreground extinction on one of the model SEDs shown in Fig. 12. A Galactic extinction curve is assumed, with the indicated magnitudes of visual extinction.

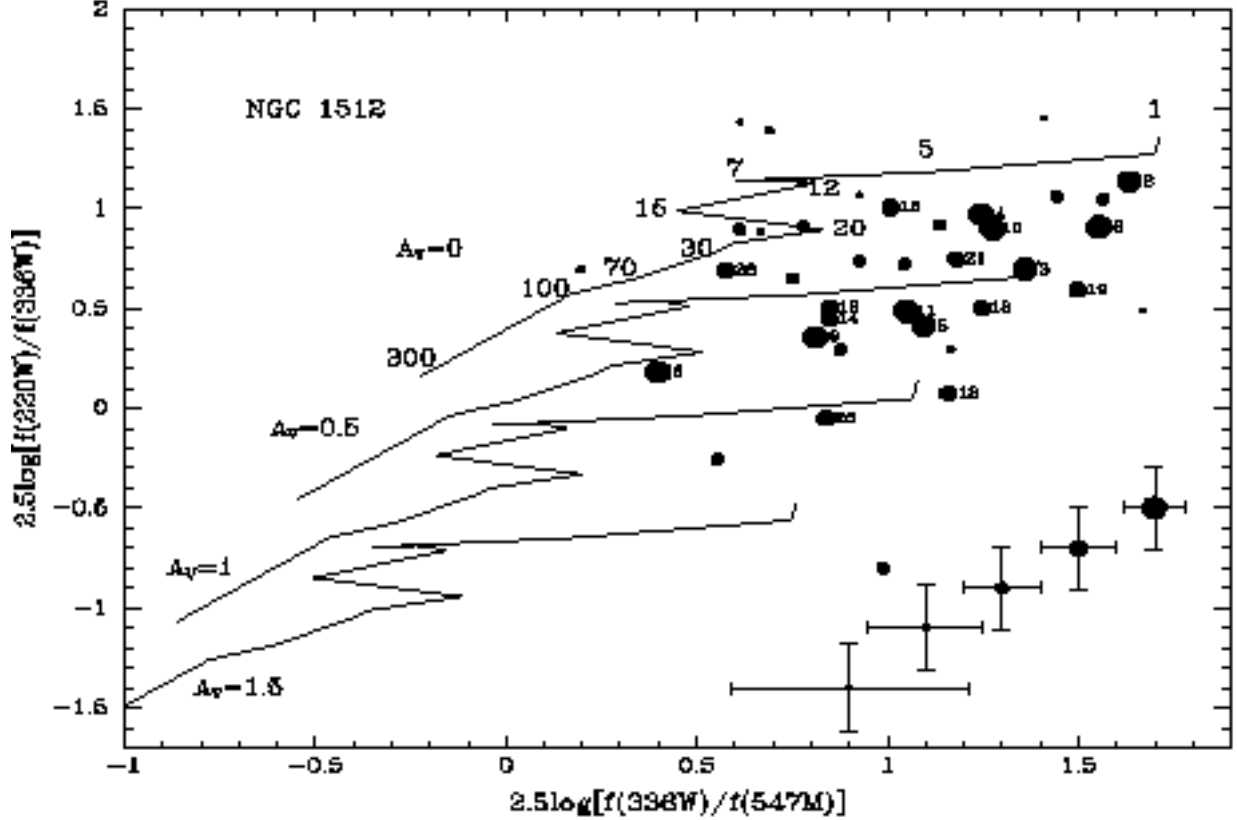
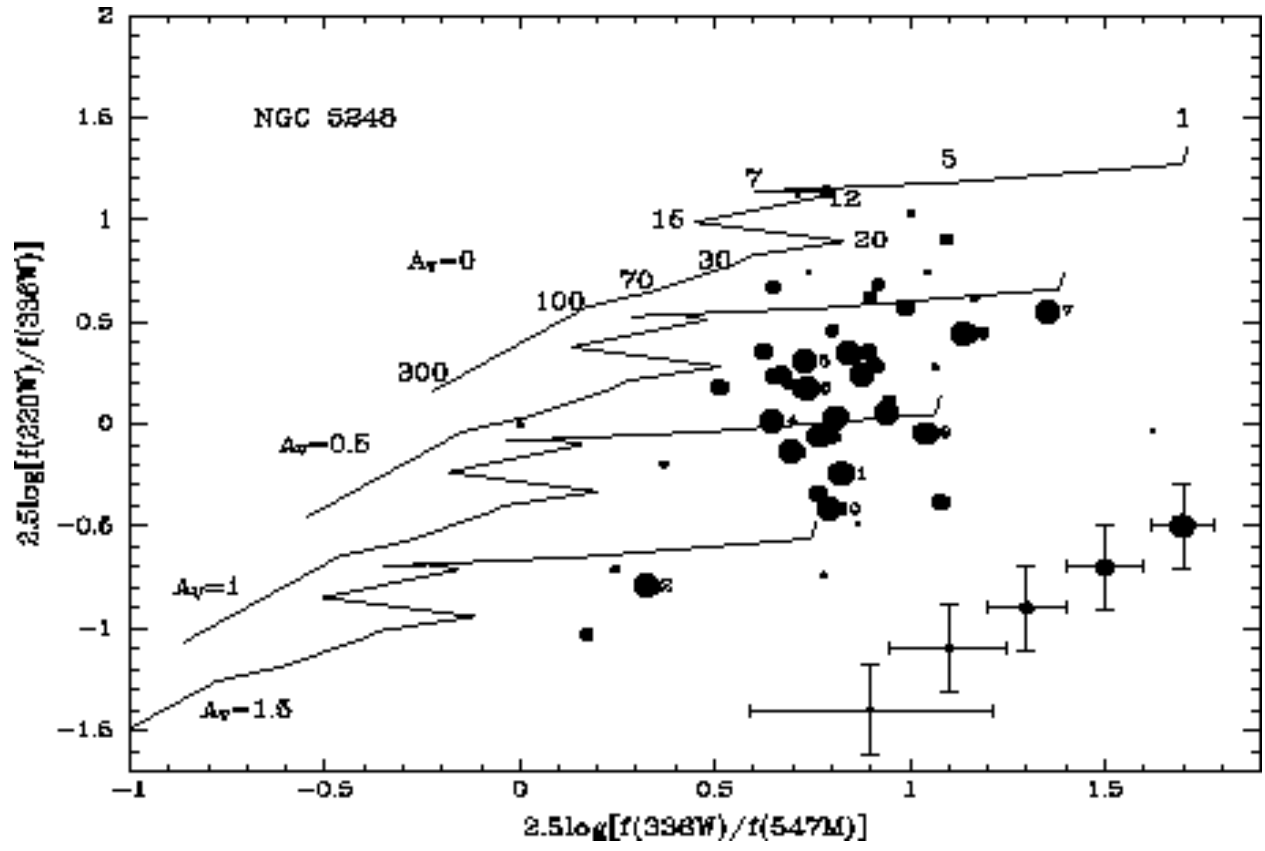


Fig. 15.— Color-color plots of  $2.5 \log[f(2300 \text{ \AA})/f(3350 \text{ \AA})]$  vs.  $2.5 \log[f(3350 \text{ \AA})/f(5490 \text{ \AA})]$  (essentially,  $U - UV$  vs.  $V - U$ ), for all sources in each galaxy that have a UV measurement. Point sizes are relative to the  $V$  brightness of each source and typical error bars for the different-sized symbols are displayed in the corner. The brightest sources are labeled with small numerals according to their designations in Tables 3 and 4. Cluster aging trajectories are shown, based on the spectral synthesis models and several values of foreground extinction. Ages in Myr are marked along the top trajectory with large numerals. The brightest clusters are young, with ages less than 5 Myr for most of the 15 brightest clusters, and less than 10 Myr for most of the UV-detected clusters in general. Extinctions are moderate, with the brightest sources clustered around visual extinctions of  $A_V = 0.5$  mag in NGC 1512 and  $A_V = 1$  mag in NGC 5248.





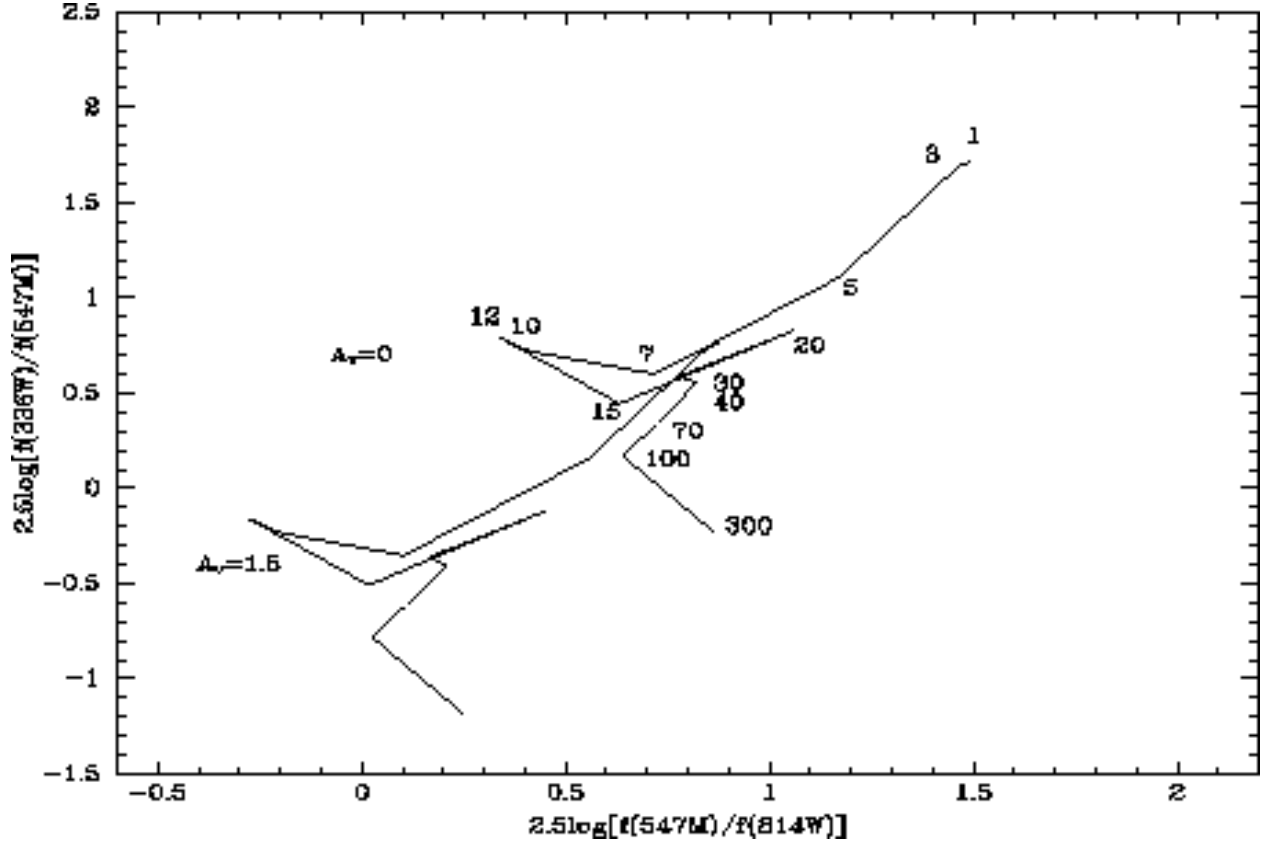


Fig. 16.— Model age trajectories for two values of extinction in the plane of  $2.5 \log[f(3350 \text{ \AA})/f(5490 \text{ \AA})]$  vs.  $2.5 \log[f(5490 \text{ \AA})/f(8040 \text{ \AA})]$  (essentially,  $V-U$  and  $I-V$ , up to additive constants). The ages, in Myr, are marked along the unreddened trajectory. The problems of backtracking and age-extinction degeneracy are evident.

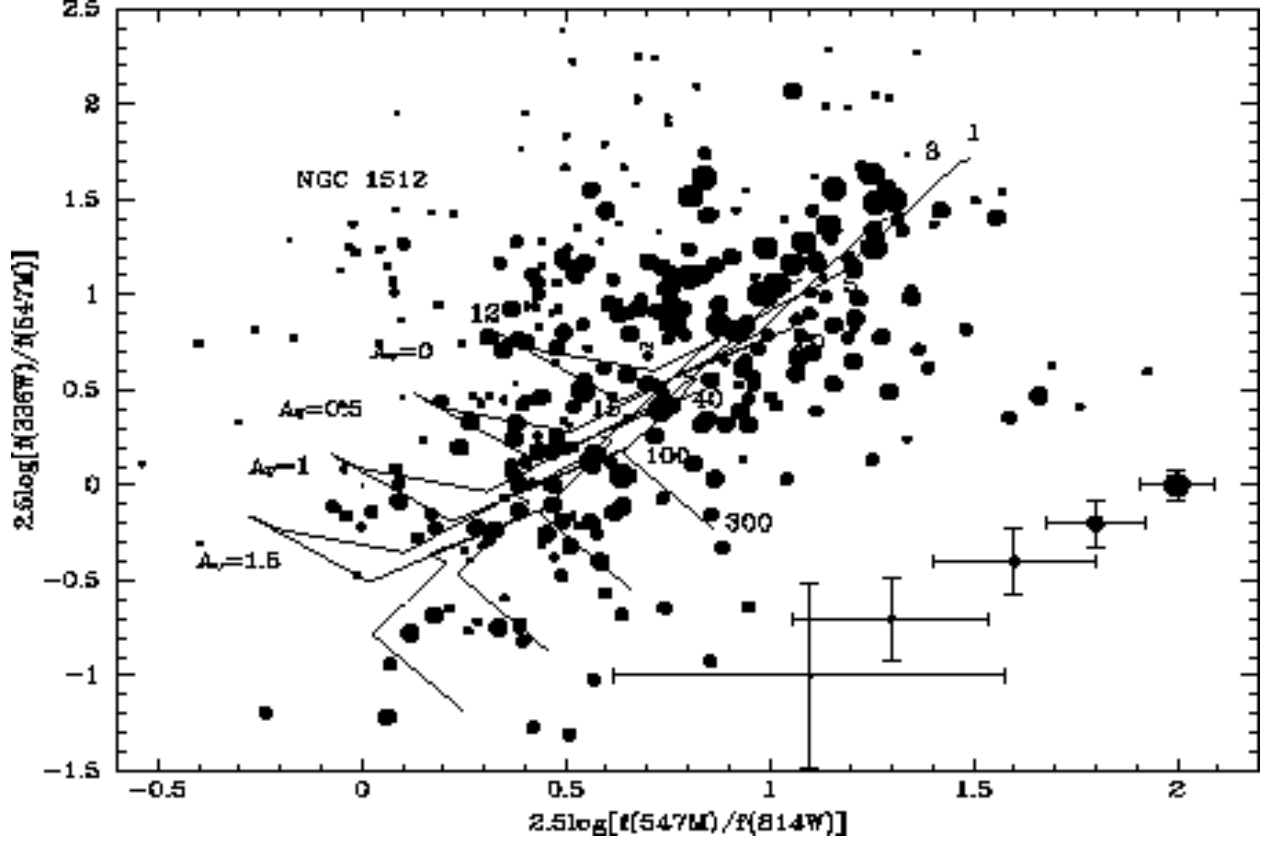


Fig. 17.— Data for all measured sources in NGC 1512 in the  $V - U$  vs.  $I - V$  plane of Figure 16. Some age labels are omitted for clarity. The 20 clusters brightest in  $V$  are shown as the largest points, and each set of the next 100 brightest sources is plotted with progressively smaller dots. Typical error bars are plotted in the corner. As in the color-color plot of Figure 15, the diagram indicates that many of the bright clusters are young and only mildly reddened.

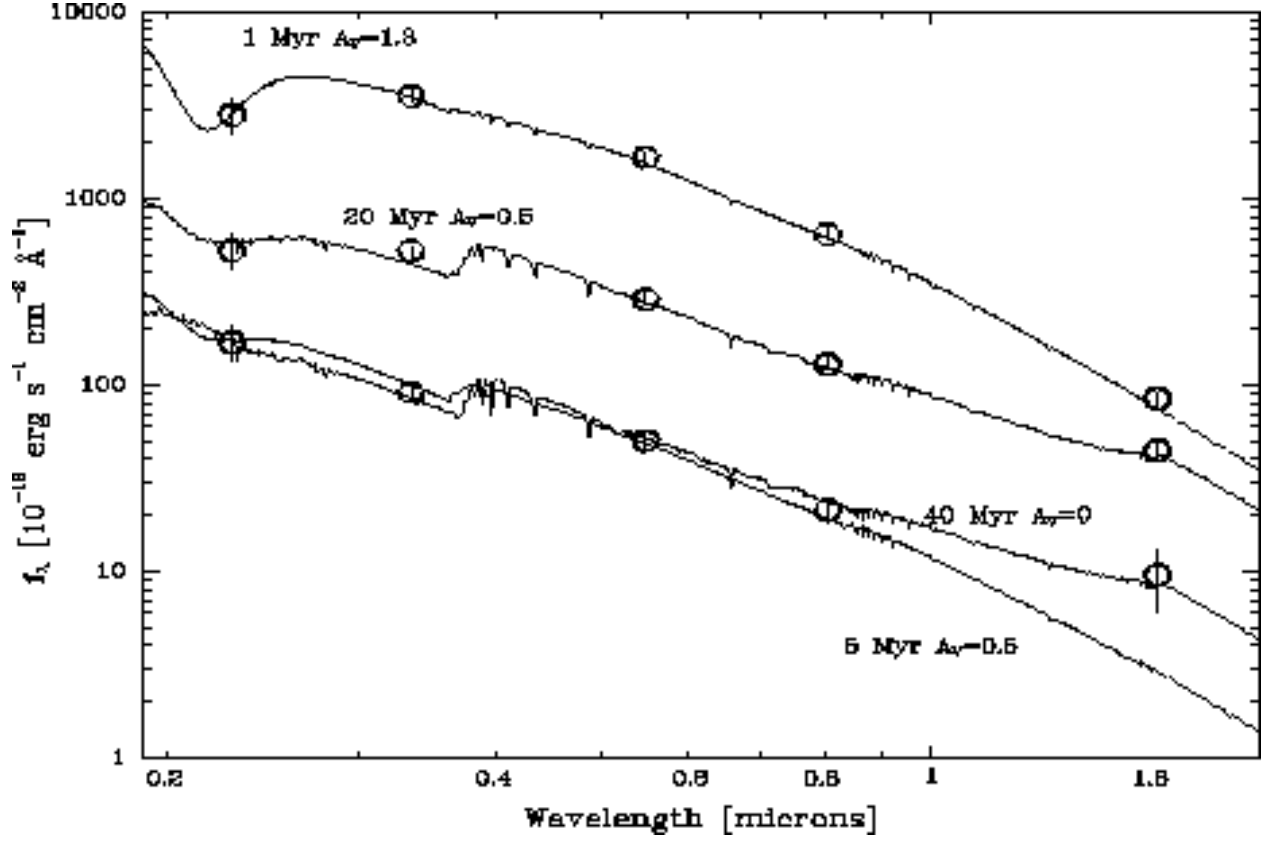


Fig. 18.— Several examples of observed cluster SEDs in NGC 5248, and their best-fitting models, with ages and extinctions indicated. For the fainter cluster, two models are shown — one that fits well, and one that is marginally consistent with the data.

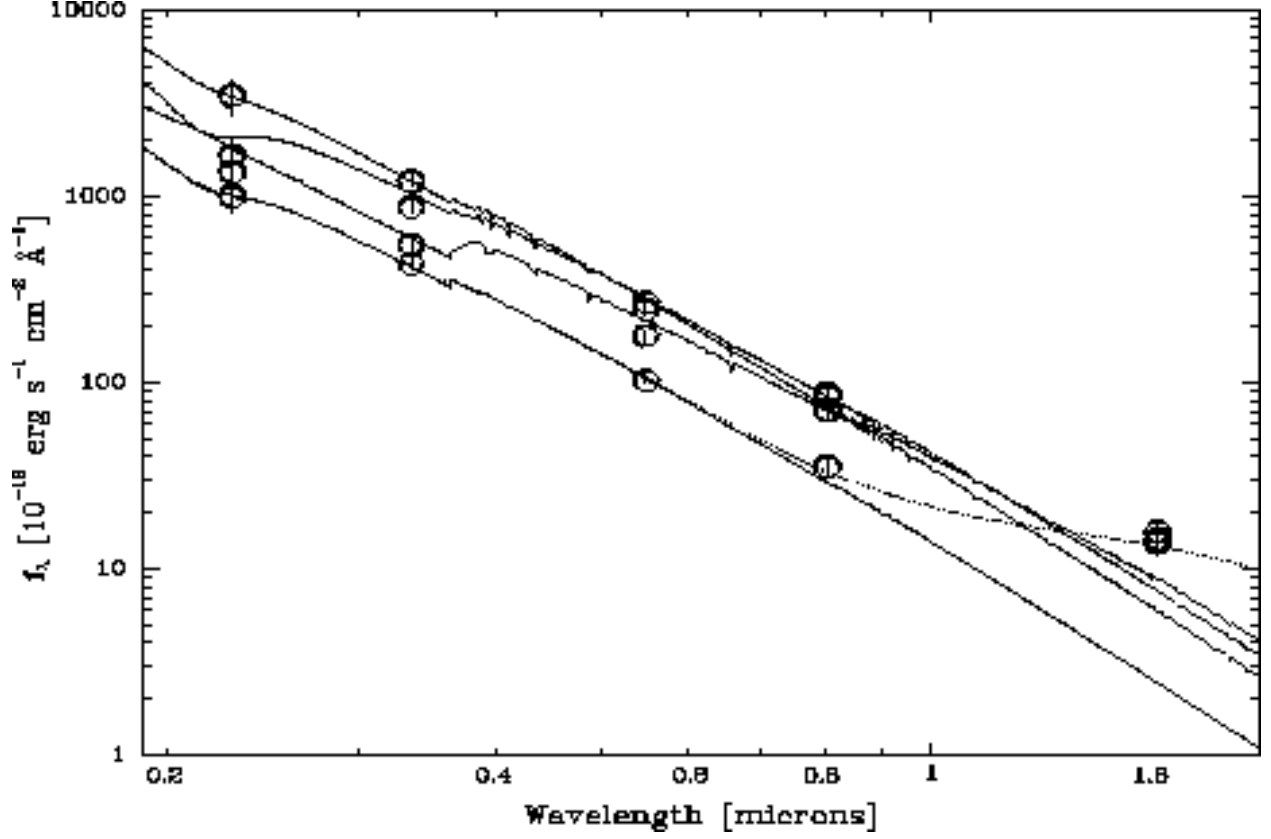


Fig. 19.— Data and best-fit models for four of the eight brightest clusters in NGC 1512. The models range in age from 1 to 5 Myr, and in extinction from  $A_V = 0$  to 0.5 mag. In many of the young and bright clusters in both galaxies, the data and models are inconsistent at  $1.6 \mu\text{m}$ . The dashed line shows the effect of adding to the lower model a 2000 K blackbody, scaled to reproduce the excess in the  $I$  and IR bands. If the excess is from dust which is heated by the cluster stars to this temperature, the dust must be circumstellar.

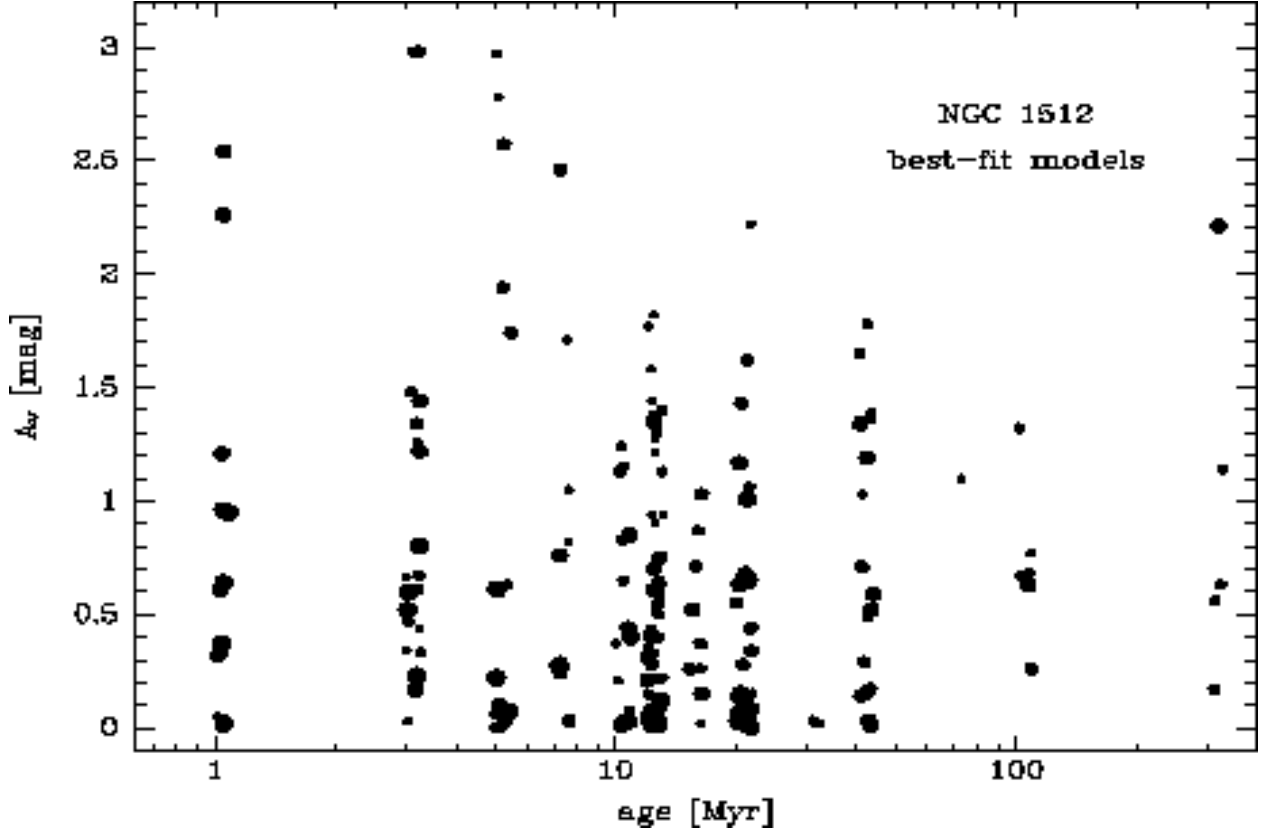
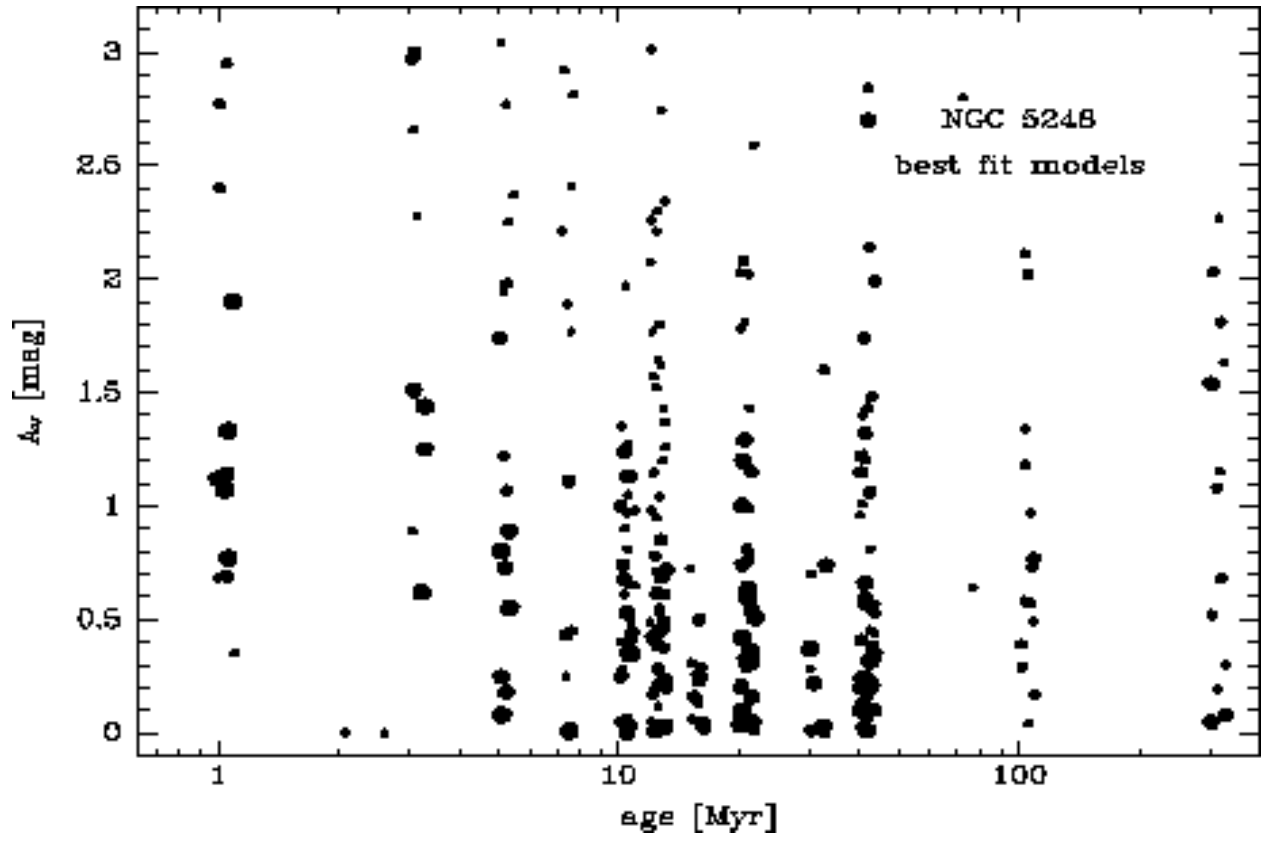


Fig. 20.— Best-fitting ages and extinctions for all sources in each galaxy having detections in at least four bands. As in the previous figures, dot size is proportional to  $V$  brightness. For most observed clusters in NGC 1512, ages  $\lesssim 20$  Myr and extinctions  $A_V \lesssim 1$  mag are indicated, with slightly greater ages and extinctions in NGC 5248. Some of the plotted best-fit models are formally inconsistent with the data. In many of these cases, however, the mismatch is due to an IR excess not predicted by the models, which still provide a good fit in the other bands.



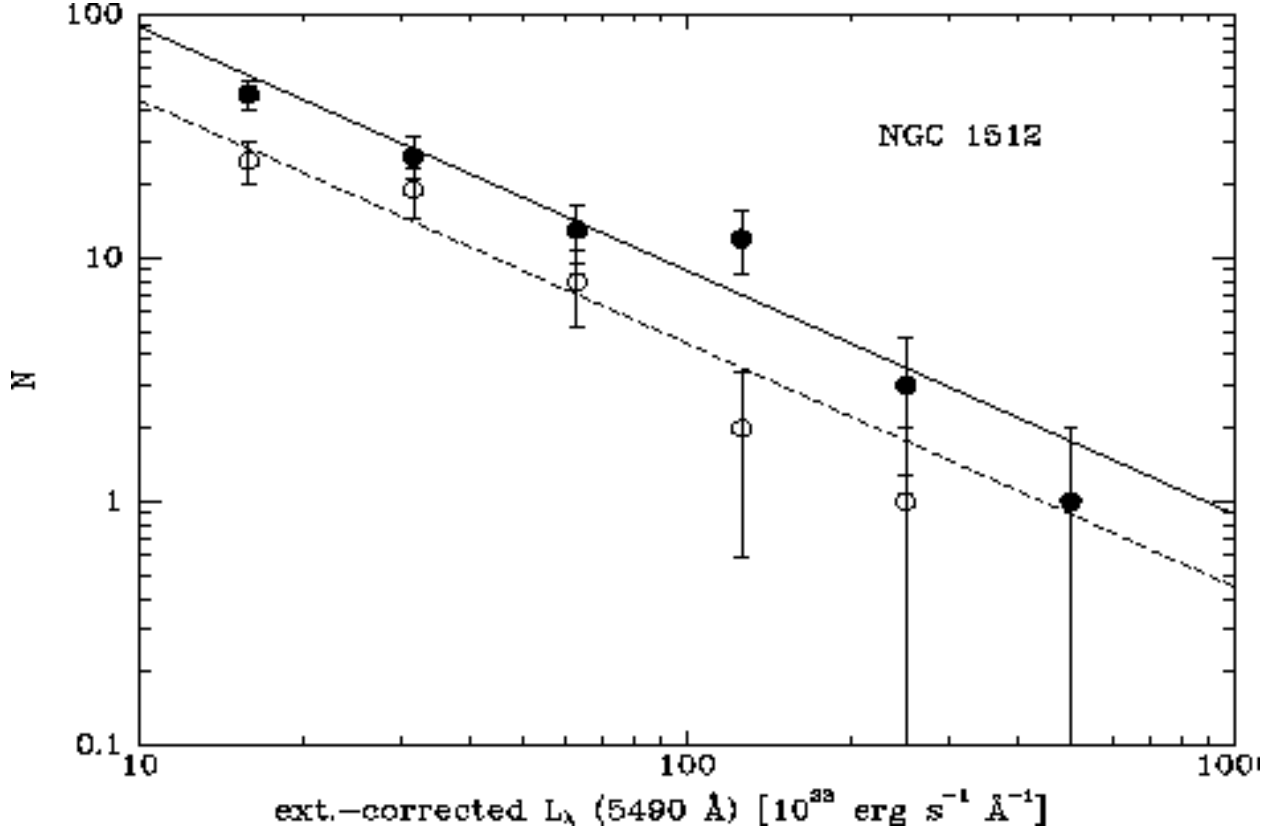
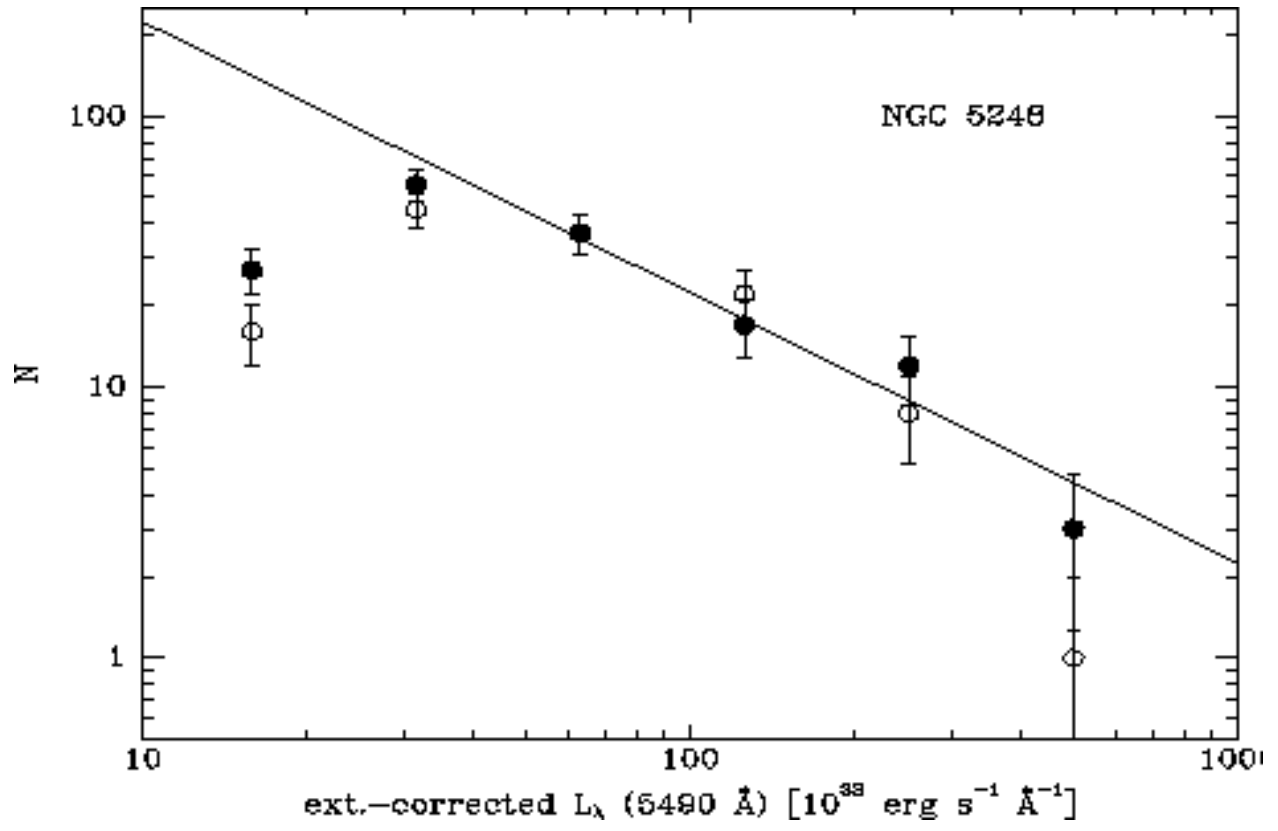


Fig. 21.— Cluster luminosity functions. Filled circles are clusters whose best-fit models have ages  $\leq 15$  Myr, and empty circles have best-fit models that are older. The  $V$  fluxes have been corrected for extinction according to each cluster’s best-fit model. Error bars are  $1\sigma$  Poisson errors. The lines are power-law distributions,  $N(L)dL \propto L^{-2}dL$ , consistent with the data in the brighter, more complete, bins. Although at any luminosity, most of the clusters are young, luminosity evolution shifts the young-cluster distribution horizontally by a factor of about 6 between ages of 10 Myr and 100 Myr (see Fig. 12). Because of the steep distribution, this creates an age bias, where young clusters are over-represented at every luminosity. After correction for this effect, the relative fractions of old and young clusters are consistent with continuous star formation in the rings, over the last  $\sim 100$  Myr.





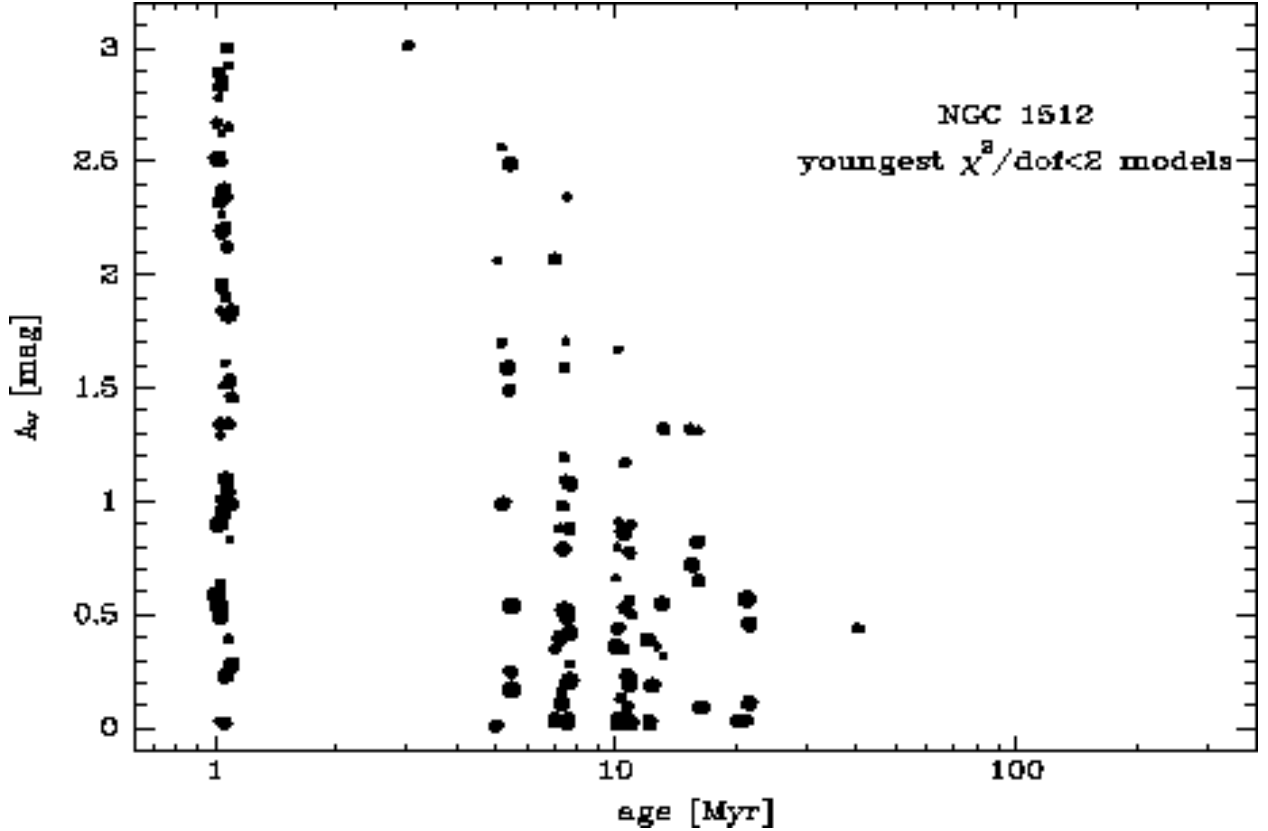
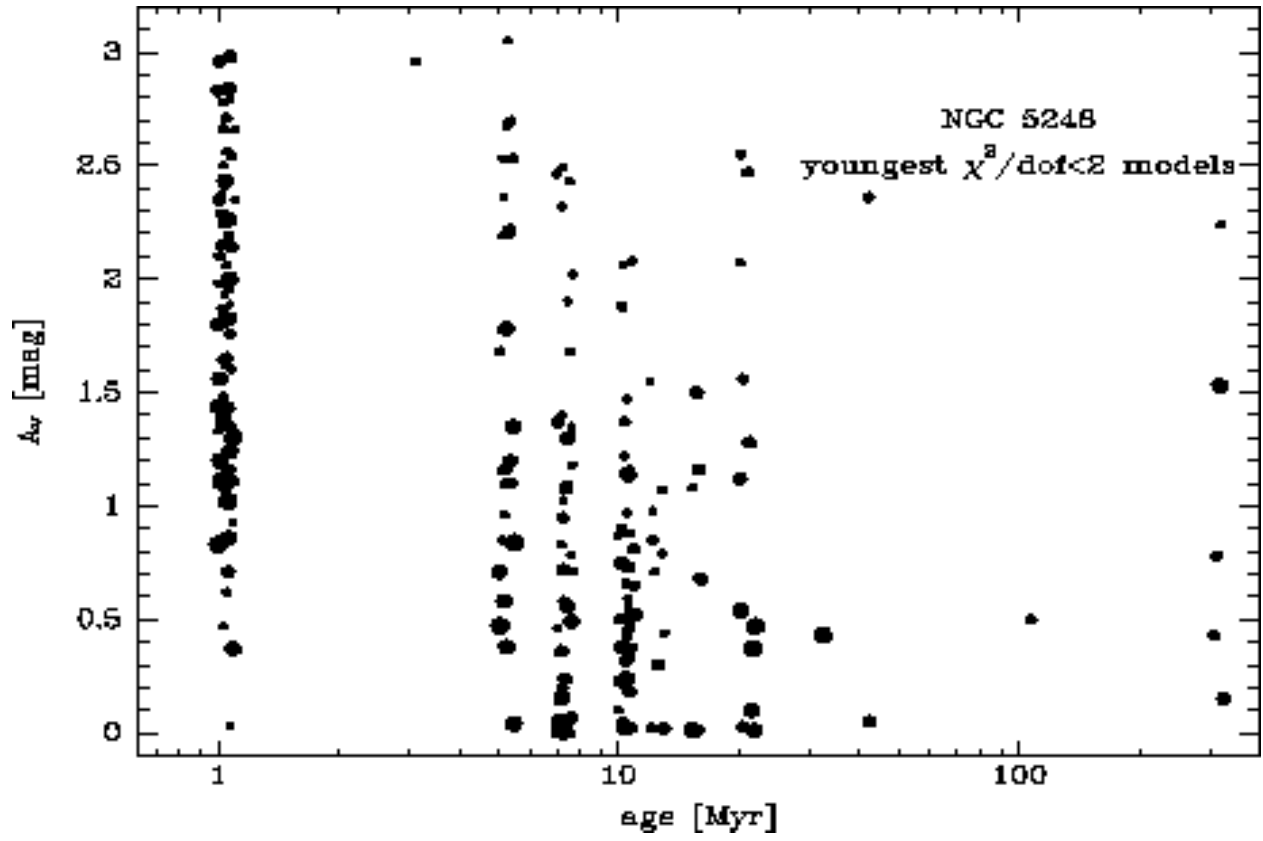


Fig. 22.— Age and extinction of the youngest acceptable model that fits each observed SED at a level of  $\chi^2 < 2$  per degree of freedom. Points are plotted only for the sources in each galaxy that have detections in at least four bands, and satisfy the above  $\chi^2$  criterion, and therefore some clusters do not appear (e.g., the bright, young clusters with an IR excess). The figures show that all but a handful of sources can be consistent with clusters of age  $\lesssim 20$  Myr. Thus, although the best fits (Fig. 20) suggest that some clusters are old, the presence of such clusters is not required by the data. The data therefore cannot distinguish between continuous and episodic star formation in these galaxies.



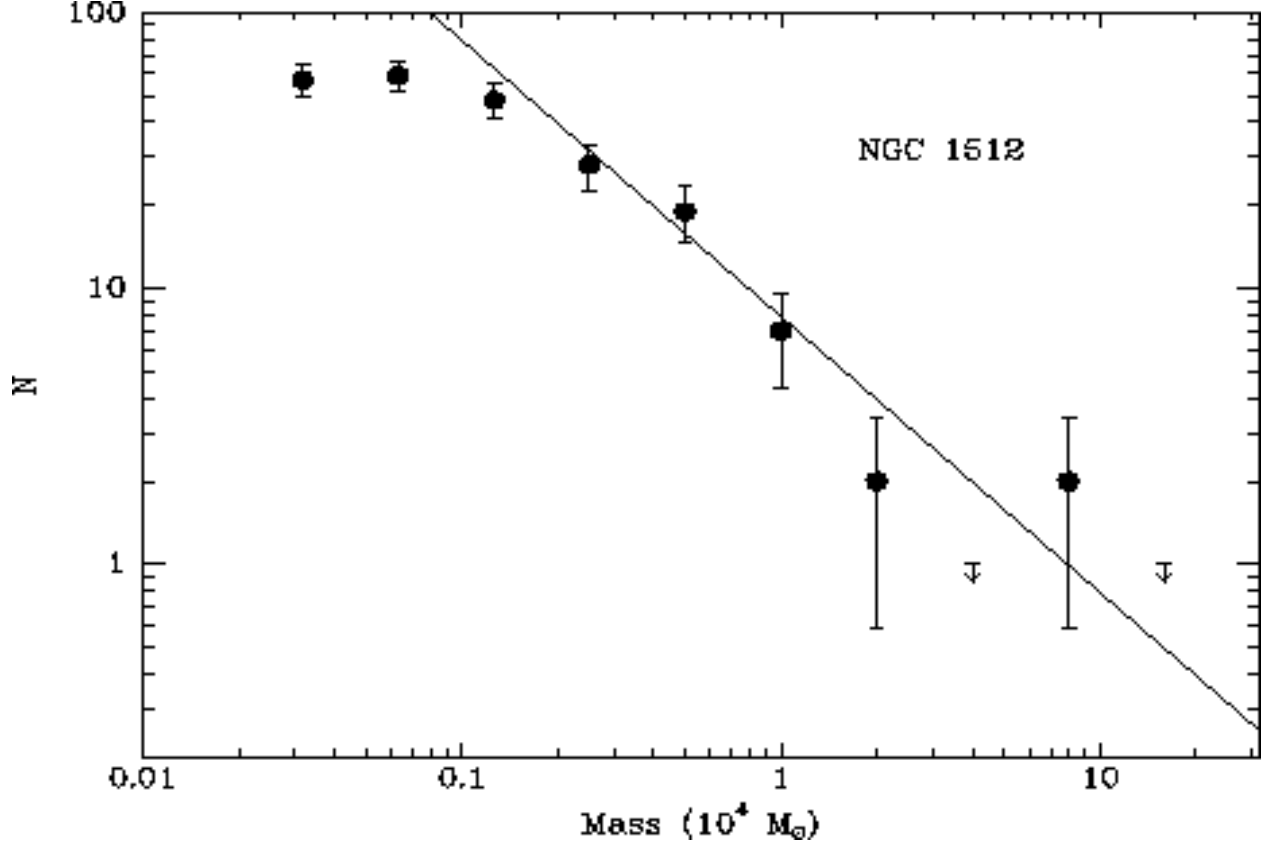
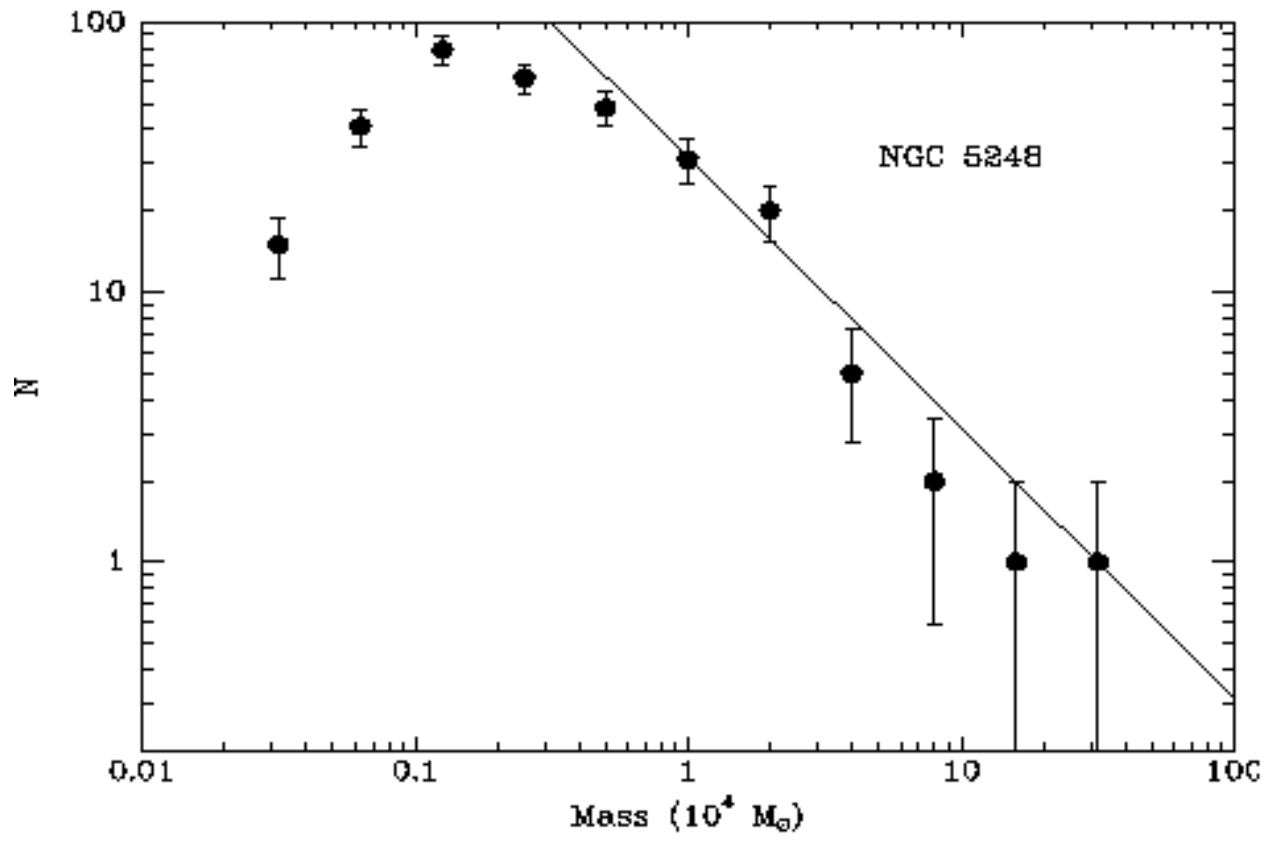


Fig. 23.— Cluster mass functions, based on the best-fit models. A  $N(m)dm \propto m^{-2}dm$  power law is drawn through the data for the more massive bins, which suffer less from incompleteness. The most massive clusters are in the range  $10^4$  to  $10^5 M_{\odot}$ . The fraction of the most massive clusters is similar to the low fractions seen in other starburst galaxies having, overall, more clusters.



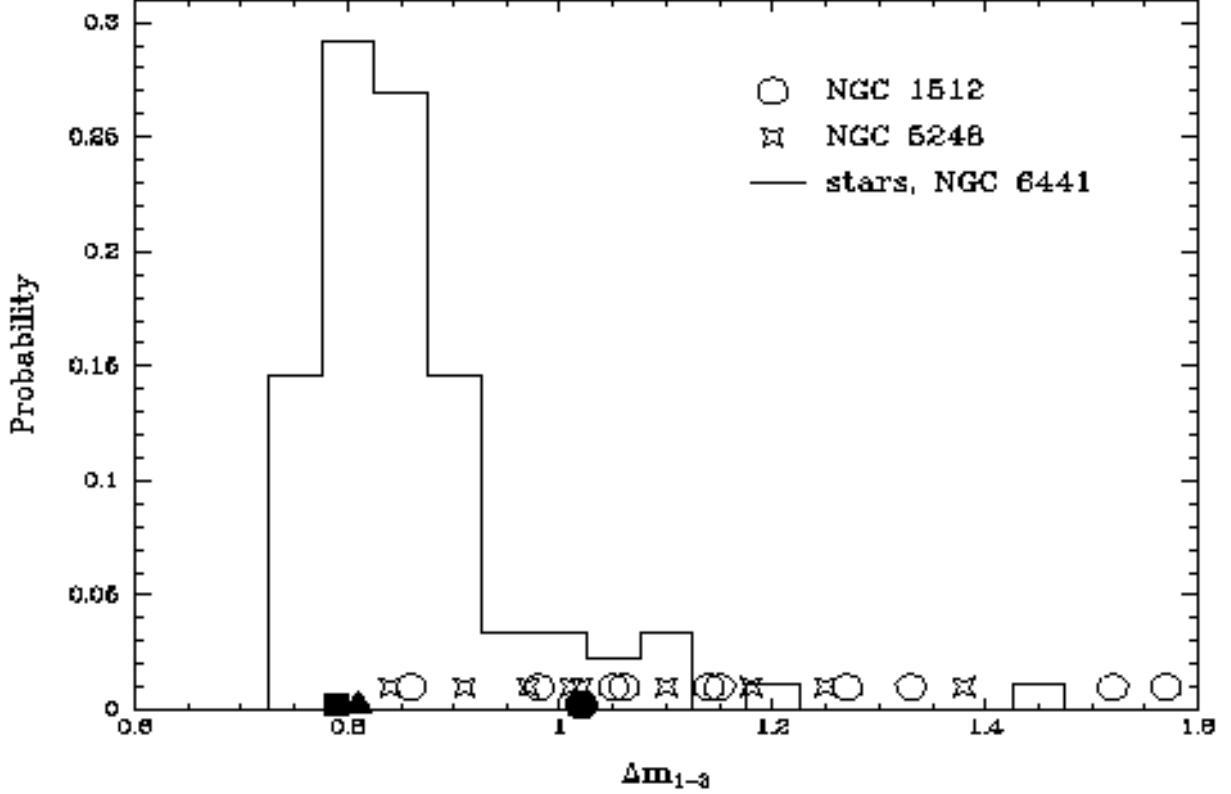


Fig. 24.— Distribution of  $\Delta m_{1-3}$  for stars in a WFPC2 F547M image of the globular cluster NGC 6441, compared with the values for the 10 brightest clusters in NGC 1512 (empty circles) and NGC 5248 (star symbols). Also shown are the two measurements based on Tiny Tim artificial PSFs, one centered on a pixel center (filled square), and one centered on a 4-pixel junction (filled circle). The filled triangle represents a red, isolated, object in NGC 1512, possibly a foreground star. The high- $\Delta m_{1-3}$  tail of the distribution for the stars encompasses many of the SSCs, rendering uncertain the degree to which they are resolved, but those with  $\Delta m_{1-3} > 1.1$  are likely resolved.

This figure "maoz.fig1.gif" is available in "gif" format from:

<http://arXiv.org/ps/astro-ph/0103213v1>

This figure "maoz.fig2.gif" is available in "gif" format from:

<http://arXiv.org/ps/astro-ph/0103213v1>



This figure "maoz.fig3a.gif" is available in "gif" format from:

<http://arXiv.org/ps/astro-ph/0103213v1>

This figure "maoz.fig3b.gif" is available in "gif" format from:

<http://arXiv.org/ps/astro-ph/0103213v1>

This figure "maoz.fig4.gif" is available in "gif" format from:

<http://arXiv.org/ps/astro-ph/0103213v1>

This figure "maoz.fig5.gif" is available in "gif" format from:

<http://arXiv.org/ps/astro-ph/0103213v1>

This figure "maoz.fig6.gif" is available in "gif" format from:

<http://arXiv.org/ps/astro-ph/0103213v1>

This figure "maoz.fig7.gif" is available in "gif" format from:

<http://arXiv.org/ps/astro-ph/0103213v1>

This figure "maoz.fig8.gif" is available in "gif" format from:

<http://arXiv.org/ps/astro-ph/0103213v1>

This figure "maoz.fig9.gif" is available in "gif" format from:

<http://arXiv.org/ps/astro-ph/0103213v1>